Development and analysis of tailored catalytic cobaltite layers for hydrogen production using electrochemical and spectroscopic techniques

Master thesis
written by Moritz Weber at

Forschungszentrum Jülich GmbH
Peter Grünberg Institute (PGI)
Electronic Materials (PGI-7)
and
Leibniz Universität Hannover (LUH)
Institute for Radioecology and Radiation Protection (IRS)

Supervised by

Prof. Clemens Walther (IRS, Leibniz Universität Hannover)
and
Prof. Regina Dittmann (PGI-7, RWTH Aachen University)

June 19th 2017 - November 30th 2017

Statement of Authorship

Moritz Weber, M. Sc. Analytik (3263170)

I hereby declare that this thesis has been composed by myself, and describes my own work, unless otherwise acknowledged in the text. All references and verbatim extracts have been quoted, and all sources of information have been specifically acknowledged.

Signed: _____

Date: _____

Contents

1 Introduction

With respect to the steady increase of worldwide energy demands [1] and the ongoing change in perspective to conventional power generation, sustainable energy technologies are in focus more than ever [2, 3]. However, increasing ambitions in renewable and climate-neutral energy production are challenging, especially because renewable energy sources (RES) are subject of high intermittency and consequently not base-load capable. Resulting from this intermittency, high RES capacities as well as efficient energy conversion and storage systems are necessary to deal with resulting energy overflows alternating with low energy production and to guarantee steady energy supply. One promising approach is the storage of energy in chemical bonds by the electrolysis of water using the incidental excess energies. However, the application of water splitting is limited by its efficiency, due the sluggish kinetics of water oxidation, demanding high potentials above the equilibrium potential. Benchmark catalysts, such as ruthenium oxide, are based on precious metals and by this are not capable for application on a large scale. As a consequence the search for earth-abundant electrocatalysts with high performance regarding to water oxidation is of particular interest for the realization of sustainable energy production.

Transition metal oxides of perovskite-type structure are promising candidates for catalyzing oxygen evolution with high activity [4, 5]. However, the lack of an universal catalysis mechanism on perovskite surfaces is hampering the material design of improved catalytic activity [6]. As a result, the search for structure-activity relationships is promoted in order to define specific criteria for the catalytic performance of perovskites. For instance the flexibility in oxidation state of transition metals is considered as one key-propertiy for their catalytic activity.

Considering the nature of perovskite catalysts, usually applied as powders, the assignment of catalytic activity to structural properties may be problematic. Differences in synthesis procedures, crystallite sizes as well as surface morphology, grain boundaries, mixed crystal orientations and additives such as carbon support may have influence to the reaction and by this hamper the determination of clear descriptors. Recent publications have shown that catalysis of water splitting in principle is possible by application of epitaxial thin film electrodes and by this the investigation of descriptors on highly defined systems [7–11].

This thesis deals with the study of $La_{0.6}Sr_{0.4}CoO_3$ (LSCO), as well established cathode material [12–14], regarding to their performance in the anodic oxygen evolution reaction. With respect to the previous considerations, epitaxial single crystalline catalytic thin films are developed, as highly defined systems for investigating the catalytic process. For this purpose, thin films of specific stoichiometry and thickness are deposited on insulating neodymium gallate by means of pulsed laser deposition. The thin film properties are studied with complementary techniques to uncover morphology, crystallography, electrical properties as well as stoichiometry and chemical

state of involved compounds. Here, one focus is the valence state of the transition metal and the potential change in the average cobalt valency, postulated as descriptor of high impact. By this procedure, a detailed picture of the applied catalyst system is obtained. Based on electrochemical experiments, the excellent electrical properties and high activities of LSCO thin films in catalyzing the oxygen evolution reaction are demonstrated. Furthermore the impact of the catalytic process to the material properties is studied. Besides morphologic and crystallographic investigations, spectroscopic measurements provide first insights to the degradation process of the electrocatalyst.

2 Fundamentals

2.1 The perovskite structure

Compounds of the formula ABO_3 are usually of the perovskite crystal structure as illustrated in figure 2.1 for a cubic perovskite oxide unit cell. Here the A-site is occupied by 12-fold coordinated alkali, alkali earth or lanthanide ions with large ionic radii, while B-side cations are typically small transition metal ions coordinated to six oxygen ions. This ideal cubic-symmetry structure forms a net of corner sharing octahedra. However the exact symmetry of the crystal structure often differs from this ideal cubic structure by a orthorhombic structure which is highly depending on the ionic radius of the involved cations. Based on variations of the type and ratio of A-site and B-site elements numerous complex perovskite compounds with the formula $A_{1-x}A'_xB_{1-y}B'_yO_{3-\delta}$ can be distinguished, where δ denotes the amount of oxygen vacancies. Here the oxidation state of the transition metal is determined by the charge and ratio of the different A-site cations as well as the stoichiometry. Consequently the transition metal of more complex perovskites commonly show mixed valency. In order to reach electroneutrality oxygen vacancies are generated or additional oxygen is incorporated to interstices of the crystal lattice when the total charge of cations deviates from +VI and the charge compensation is not possible by the change in oxidation state of the transition metal cation. Especially transition metal oxides have a disposition to form high concentrations of oxygen vacancies which have a major impact on the physical, chemical and electronic properties of the materials [6, 15].

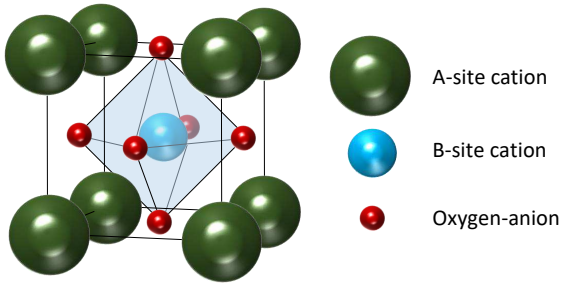

Figure 2.1: Cubic ABO_3 unit cell of the perovskite crystal structure.

$NdGaO_3$ (NGO)

Neodymium gallate ($NdGaO_3$, NGO) is an insulating rare-earth perovskite with neodymium (+III) as A-site and and gallium (+III) as B-site cation. By transformation of the orthorhombic lattice constants of $a = 5.43$ Å, $b = 5.50$ Å and $c = 7.71$ Å [16], the crystal structure can be considered as pseudo-cubic with a lattice parameter constant of $a_0(\mathrm{NGO}) = 3.86$ Å. Thus NGO crystals with (110) orthorhombic and corresponding (001) pseudo-cubic surface termination are common substrate materials for the growth of cubic oxide thin films [17]. The thermal expansion parameter of NGO is $\frac{\partial a}{\partial \mathrm{T}}|_\delta = 9 \cdot 10^{-6}\ \text{Å} \cdot \mathrm{K}^{-1}$ [16].

$La_{0.6}Sr_{0.4}CoO_3$ (LSCO)

Lanthanum strontium cobalt oxide ($La_{0.6}Sr_{0.4}CoO_3$, LSCO) is a mixed conducting transition metal oxide with an orthorhombic crystal structure. While 60 % of the A-sites of the perovskite is occupied by lanthanum (+III) and 40 % are occupied by strontium (+II), cobalt is the only B-site cation. Compensating the remaining 3.4 charges, assuming no oxygen deficiency, the cobalt ion can occur in the mixed formal oxidation states of +II, +III and +IV. Just as NGO, the LSCO crystal structure can be described as pseudo-cubic with a lattice parameter constant of $a_0(\text{LSCO}) = 3.8131$. The thermal and chemical expansion parameter is $\frac{\partial a}{\partial T}|_\delta = 6.124 \cdot 10^{-5}$ Å $\cdot \text{K}^{-1}$ and $\frac{\partial a}{\partial \delta}|_T = 0.0827$ [18]. The lattice mismatch between NGO and LSC is about 1.3 %.

2.2 Epitaxy

In this section the characteristics of epitaxial thin film growth, with special focus on heteroepitaxial thin films are briefly depicted.

For the growth of single-crystalline thin films, materials are usually deposited on crystalline substrates of the same material (homoepitaxy) or on materials with a crystal lattice in the same order as the film material (heteroepitaxy). In contrast to homoepitaxial grown films, heteroepitaxial growth always involves a misfit f between the crystal lattices given by equation 2.1

$$f = \frac{a_0(substrate) - a_0(film)}{a_0(film)} \tag{2.1}$$

where a_0 denotes the unstrained bulk reference lattice parameter. Unless the energy related to an accommodation of the interatomic spacing of the materials does not exceed the energy of the relaxed lattice structure the film grows strained. Compressive ($f < 0$) or tensile ($f > 0$) strain can be distinguished. Assuming a constant volume of the materials unit cell, decreased in-plane lattice parameters resulting from compressive strain will lead to a an increase in the out-of-plane lattice constants. Vice versa decreased out-of-plane lattice constants are a consequence of tensile strain.

The strain energy and by that the probability for relaxation of the crystal lattice is additionally depending on the materials characteristics, such as thermal expansion coefficients of the materials as well as deposition parameters and film thickness [19]. Another possibility to compensate the energy introduced in the crystal lattice is the formation of defects at the substrate-to-film interface as well as within the whole thin film lattice. All defects such as vacancies, dislocations or grain boundaries lead to deviations from the ideal periodic crystal lattice and by that alter the materials properties.

Due to the fact the perovskite structure is favourable towards oxygen vacancy formation, relatively high amounts, denoted by δ as described above, can result from thin film growth. Here the properties of B-site cations are of high impact for the probability of vacancy formation [20].

2.3 Oxygen evolution reaction

This section provides a brief introduction to the basic principle of the oxygen evolution reaction (OER) as well as the recent approaches to overcome its kinetic limitations.

Water splitting i.e. the decomposition of water molecules to hydrogen and oxygen gas proceeds in two half-reactions namely the oxygen evolution reaction (OER) and the hydrogen evolution reaction (HER). For alkaline media the reaction is given by equation 2.2 and 2.3.

$$4\,OH^- \longrightarrow O_2 + 2\,H_2O + 4\,e^- \tag{2.2}$$

$$4\,H_2O + 4\,e^- \longrightarrow 2\,H_2 + 4\,OH^- \tag{2.3}$$

As can be seen HER is a two electron-transfer reaction, while OER is a four electron-proton coupled reaction. Thus water splitting is hampered especially by the sluggish kinetics of the multi-step oxygen evolution reaction and operational potentials greater than the equilibrium potential of 1.23 V are necessary for sufficient reaction rates. For the reduction of overpotential i.e. the difference between operational and equilibrium potential required to yield a specific exchange current density, the application of catalysts is necessary. Here perovskite-type transition metal oxides, showing high catalytic activities relative to conventional precious metal based catalysts, are of particular interest. The four electron transfer steps of the reaction are shown for alkaline media, starting from the resting state between catalyst and electrolyte (no voltage) by the following equations [5]. Here M denotes the transition metal active site at the perovskite surface.

$$MOH + OH^- \longleftrightarrow MO + H_2O + e^- \tag{2.4}$$

$$MO + OH^- \longleftrightarrow MOOH + e^- \tag{2.5}$$

$$MOOH + OH^- \longleftrightarrow MOO + H_2O + e^- \tag{2.6}$$

$$MOO + OH^- \longleftrightarrow MOH + O_2 + e^- \tag{2.7}$$

Similar to metal catalysts, oxidic catalysts are proposed to promote the OER by adsorptive interaction with the different intermediates of each reaction step facilitating charge transfer. This adsorptive approach, considering the surface as simple extension of the perovskite structure was postulated by Goodenough et al. as illustrated for cobalt as active site in figure 2.2. As can be seen, the meachanism is based on alternating redox reaction so the transition metal, where the intermediates of OER originate from the electrolyte.

Due to the lack of an universal mechanism describing the catalysis process and the great variability of perovskites and hence the wide range of (catalytic) properties, numerous investigations were done to find criteria for the design of efficient catalyst materials. Over the course of time various descriptors, connecting structural and electronic properties of perovskite oxides to their catalytic activity regarding oxygen evolution related to bulk as well as surface properties for the catalytic activity were observed. For instance correlations of the enthalpy for the transition to a higher oxidation state, the enthalpy for the formation of transition metal hydroxides, the point of zero charge, the d-electron number as well as the band alignment with the catalytic activity were found. All these parameters were connected to the optimal interaction strength between reactant and catalyst and by this are with influence to the reaction [4].

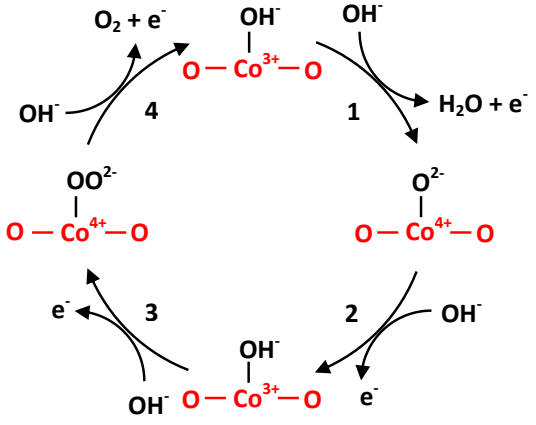

Figure 2.2: Adsorbate evolution mechanism for the catalysis of OER at perovskite-type surfaces, illustrated by taking the example of cobalt as active site undergoing the catalytic redox reaction. The order of reaction steps, equal to equations 2.4 - 2.7 is given in arabic numbers. Red symbols denote species of the perovskite lattice, blue symbols denote species of the electrolyte (see [21]).

Furthermore non-stoichiometry in oxide catalysts, were stated to be of particular importance for the catalytic activity. Besides deficiency or excess of material components the concentration of oxygen vacancies was shown to strongly affect the catalytic activity [6] and was recently the occasion for the postulation of a novel, lattice-oxygen mediated catalysis mechanism (LOM) [21].

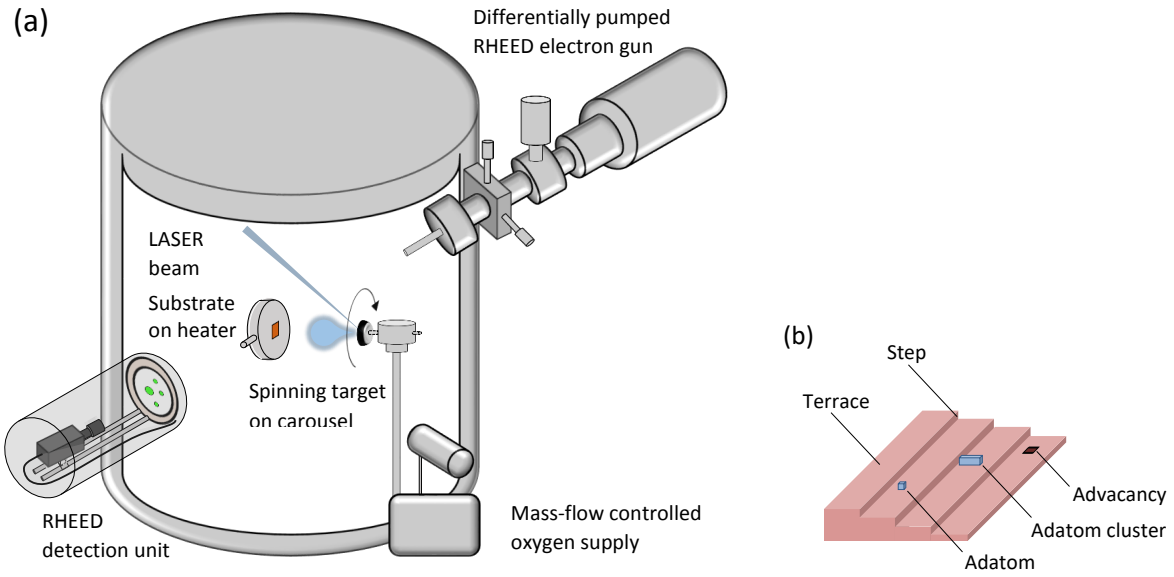

Figure 2.3: (a) Schematic design of a PLD system pristine and (b) surface terrace step structure of an annealed substrate.

2.4 Experimental methods

The following section provides a brief overview of the basic principles of preparative and analytic techniques applied in the further studies.

2.4.1 Thin film preparation

2.4.1.1 Pulsed Laser Deposition (PLD)

As a technique for the fabrication of thin films at controlled pressures pulsed laser deposition (PLD) allows the growth of complex, multielemental oxides. The thin film properties are controlled based on the variation of several deposition parameters. In this way, growth kinetics can be manipulated and consequently material properties can be tailored precisely with respect to its subsequent application. Film preparation by PLD is realized by directing short, high-energetic laser pulses on a ceramic target located in a vacuum chamber for the ablation of bulk material as illustrated in figure 2.3 (a). As a result of multiphoton ionization processes a plasma plume is generated which provides the subsequent transport and deposition of the target particles on the substrate surface. Due to conversion of the initial thermal and ionization energy to kinetic energy the plasma expands towards the substrate positioned in parallel to the target. During plasma expansion collisions with the ambient gas molecules cause a decrease in kinetic energy with high impact on the following nucleation on the substrate surface. Due to the fact that deposition time usually is short compared to diffusion time, deposition and nucleation process can be considered as separate processes [22].

In general film growth starts from energetically advantageous locations such as terrace step edges of the crystalline substrate, shown in figure 2.3 (b). Here the typical morphology of an atomically flat single crystal surface, manifested in a clear terrace step structure along its crystallographic

orientation, as well as adatoms, adclusters as well as advacancies resulting from the deposition process are illustrated. However accessibility of certain locations at the substrate surface and by that the growth mode and eventually film morphology depends on the energy of the adspecies as well as the surface and interface energies of the materials. Starting from homoepitaxial growth Frank-van-der-Merwe or layer-by-layer growth, Volmer-Weber or 3D-island growth can be distinguished. In heteroepitaxial film growth, additional energy is introduced in the system by means of strain in consequence of slight misfits between substrate and film lattice parameter and differences in the thermal expansion coefficients. Here Stranski-Krastanov growth a form of mixed layer and island film growth can occur. Besides other kinetic parameters, the surface diffusion length has a great impact on the growth mode determining the ability of intra- and interlayer diffusion. In case of high mobility of adatoms, facile intralayer diffusion lead to successive growth, starting from the terrace step edges, while nucleation in the center of terrace steps is hindered. When intralayer diffusion is low, this step-flow growth mode is not possible and nucleation in the center of terrace steps and consequently island growth is likely. In this case film morphology depends on the ability of interlayer diffusion. Facile interlayer diffusion enables easy detachment of adatoms from the multilayer and by this layer-by-layer growth [23]. Most basic parameters for the control of growth kinetics are gas pressure, laser fluence and substrate temperature, however different deposition parameters can not be considered as independent. While the magnitude of gas pressure mainly determines the mean free path length of the ablated species as well as the amount of incoorporated atoms which do not stem from the target itself, the substrate temperature determines the ability of surface diffusion of the deposited species. High substrate temperatures promote the diffusion, while low temperatures limit intra- and interlayer diffusion and lead to formation of adatom-clusters of low mobilities. Mass- and energy-dependent scattering of the different elements of the target material will influence the composition of the generated plasma. Thus, laser fluence can be used to tune the stoichiometry of the ablation and deposition process.

2.4.1.2 High-Pressure Reflection High-Energy Electron Diffraction (RHEED)

The growth process is monitored by high-pressure reflection high-energy electron diffraction (RHEED) capable for use under controlled pressures up to one millibar. Here an electron beam, generated by a differentially pumped electron gun, is focused on the sample surface under a grazing incident angle. The resulting specular spot and diffraction pattern is displayed on a phosphor screen and gives information about both, surface roughness and ordering of first layer atoms, based on intensity and positioning of the pattern. Typical electron energies of $E = 25$ keV lead to wavelengths below $\lambda < 0.1$ Å. Considering grazing incident, the effective energy in direction to the surface ensures extraordinary surface sensitivity.

While the intensity and positioning of the diffraction spots depend on the nature and structure of the crystal lattice, described by Laue condition, their relative intensity is varying during the thin film growth. Alternating surface roughness during the formation of one unit cell and flattening due to completion of one unit cell layer leads to an periodically variation of RHEED intensity as shown in figure 2.4 where the intensity is schematically illustrated depending on the coverage rate of the surface. Albeit this ideal intensity response to film growth is unrestricted only valid

process rheed version1.pdf process rheed version1.pdf

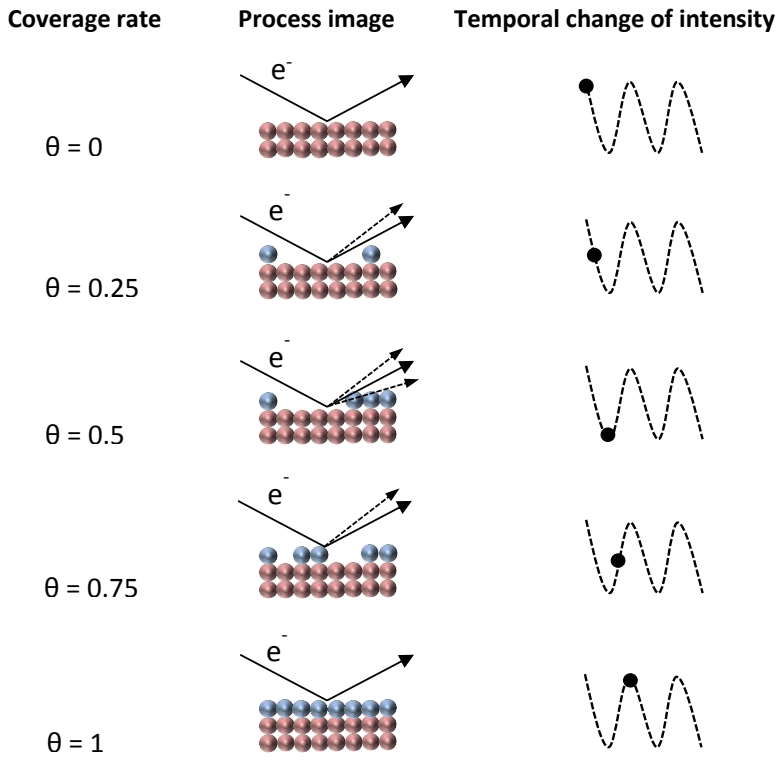

Figure 2.4: Illustration of RHEED oscillations depending on coverage rate during layer-by-layer growth.

for layer-by-layer growth, the resulting oscillating signal gives information about the growth rate [24]. Besides this valuable information to control thin film thickness, changes in RHEED pattern such as broadening of spot size or shifts of spot positions give in-situ information about the surface structure, e.g. roughness or defects and by this about the growth mode. [23]

2.4.2 Crystallographic and morphologic characterization

2.4.2.1 AC mode Atomic Force Microscopy (AFM)

Atomic force microscopy (AFM) allows the analysis of surface morphologies, based on the interaction of a silicon tip functioning as probe with the sample surface. Besides high resolution topological images this technique provides characteristic parameters such as the surface roughness. Various AFM scanning modes, using different approaches to gain information about the sample can be distinguished, where AC- or tapping mode is well established for analysis of samples in ambient conditions, since it exhibits increased signal-to-noise ratios. As shown in figure 2.5 (a) the basic components of an AFM are the x-y-z-sample stage, an optical microscope, the probe system consisting of a piezoelectric element a cantilever and a probing tip, as well as an optical detection system.

In dynamical AC-mode the sample is scanned by a silicon probe attached to a elastic cantilever, while the cantilever is mechanically oscillating in the vicinity of the sample close to its first resonance frequency using a piezoelectric element. During the measurement the cantilever basis

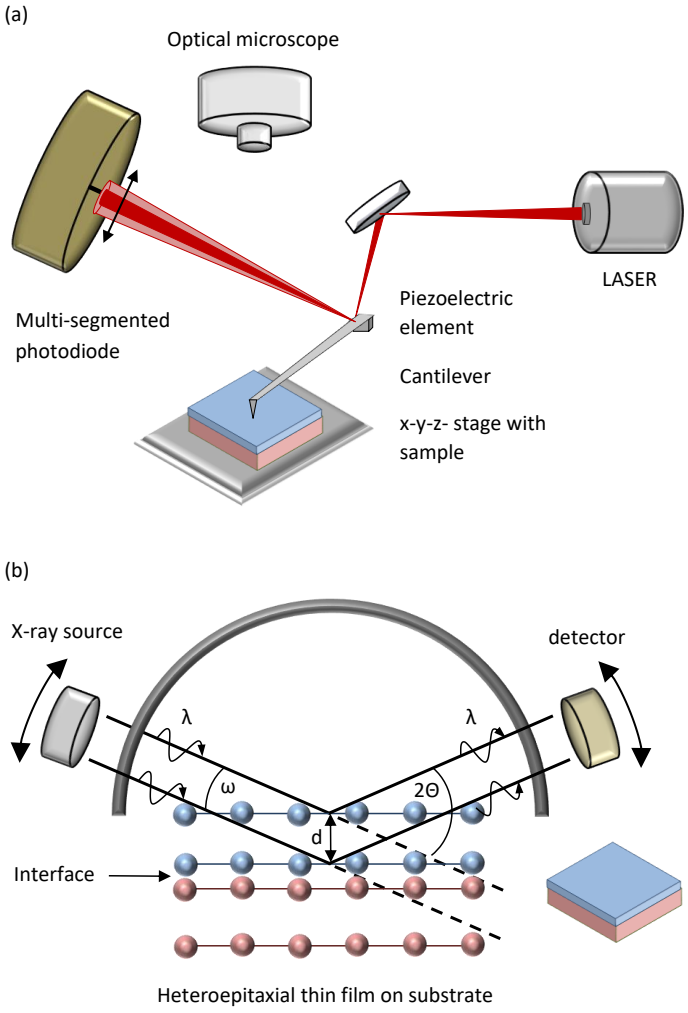

Figure 2.5: Schematic design of an (a) atomic force microscope and (b) x-ray diffractometer.

is in a fixed distance relative to the surface. Monitoring the deflection of a laser beam focused on the cantilever with a multiple segmented photodiode enables the determination of oscillation amplitude and phase. Variations in sample topography affects the amplitude by interaction with the changing force field, depending on the distance between tip and surface atoms. While at large distances between oscillating tip and sample the oscillation is not influenced, attractive interaction e.g. due to van-der-Waals force and in decreasing distance repulsive interaction e.g. due to Coulomb repulsion change the characteristics of the cantilever oscillation. Due to the fact, the amplitude is linearly depending on the z-position of the tip relative to the sample surface, the tip-to-sample distance can be adjusted by defining the amplitude set-point [25].

The differences between drive oscillation and detected oscillation amplitudes give information on the forces acting on the tip. Similarly resulting changes in oscillation phase and frequency give information about the strength of interaction and by this about the surface topography.

2.4.2.2 X-Ray Diffraction (XRD)

X-ray diffraction measurements, based on the reflection of x-rays on crystallographic planes, give information about the lattice structure of a crystal. Here x-rays of a defined wavelength are directed on the sample in a specific incident angle to the surface while the detector is scanning the diffraction signals in a distinct angular range. Reflection on adjacent crystallographic planes causes a path difference and by that a difference in phase. Whether the resulting interference of the outgoing waves is constructive or destructive depends on the extent of path difference and consequently on the interplanar spacing d. This condition is described by Braggs law 2.8

$$n \cdot \lambda = 2 \cdot d \cdot sin(\Theta) \tag{2.8}$$

where λ is the wavelength, Θ is the incident angle of the x-ray beam and n is an integer, denoting diffraction order. After calculation of d-spacing based on Braggs condition the lattice constant d_{hkl} with Miller indices (hkl) for a cubic crystal system can be determined by taking account of its geometry.

$$d_{hkl} = d \cdot \sqrt{h^2 + k^2 + l^2} \tag{2.9}$$

Using this technique, measurements performed symmetric to the crystal planes for instance in 2 Θ/Θ-geometry give information about the out-of-plane- or c-lattice constant.

Analysis with additional information about the in-plane- or a-lattice constant are possible using asymmetric measurements such as reciprocal space mapping (RMS). Involving high-index crystallographic planes, RMS is performed by repeated scans while ω (half the scattering angle) is successively offset for each scan by a specific angle $\delta\omega$ from the previous [26]. Using this method, diffraction signals give information about both, in-plane and out-of-plane spacing. Hence decomposition of the signal is necessary to separate the contributions of the different planes as described by equations 2.10 and 2.11.

$$a = \frac{1}{1/\lambda \cdot (cos(\omega) - cos(2\Theta - \omega))} \cdot k \tag{2.10}$$

$$c = \frac{1}{1/\lambda \cdot (sin(\omega) - sin(2\Theta - \omega))} \cdot l \tag{2.11}$$

Furthermore thickness fringes due to interference of the diffracted beam based on the change in refractive index between film and substrate material can be used to estimate film thickness using equation 2.12

$$t = \frac{(i - j) \cdot \lambda}{2 \cdot (sin(\omega_i) - sin(\omega_j))} \tag{2.12}$$

where i and j are the fringe orders [27].

2.4.3 Electrical and electrochemical characterization

2.4.3.1 Four-point probe resistivity measurement

For many applications electrical properties of thin film materials are of great importance and low resistivity is required when using them in electrical circuits. Thus, the determination of the exact resistivity of the material is one essential part of thin film characterization.

The thin films' resistivity can be determined by four-point probe measurements in Van der Pauw configuration as illustrated in figure 2.6. By means of this absolute technique the specific resistivity of arbitrary shaped samples are obtained if the requirements of an uniformly thick sample, an utterly intact surface and sufficiently small contacts along the outer edge of the sample are complied. In general the measured resistivity is influenced by the sample shape and thickness as well as the geometry of probes and properties of contact material. Based on the multiple measurements with alternating contacts for current flow and determination of potential difference the influence of contact and wire resistance, which can be of the same magnitude as the sample resistance, are removed. This so-called configuration switched method furthermore allows the correction of influence of contact geometry and sample shape, since the error is a function of the ratio of sample side length and contact size [28]. A widely used measure to characterize thin film resistivity is the sheet resistivity which can be directly obtained from Van der Pauw measurements by taking the thin film thickness into account. Due to this normalization to film thickness the sheet resistivity ρ_S $[\Omega \cdot \square^{-1}]$ is a suitable parameter to compare the electrical properties of different thin film materials [19]. Subsequent measurement with switched contact ordering, for example 1 (V-), 2 (V+), 3 (I-), 4 (I+) and 1(I-), 2 (V-), 3 (V+), 4 (I+) leads to the resistances

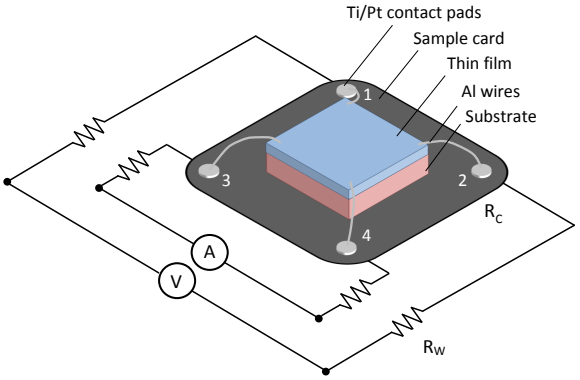

Figure 2.6: Principle design of the four-point-probe measurement geometry in Van der Pauw configuration.

$$R_{12,34} = \frac{V_{12}}{I_{34}} \quad and \quad R_{23,14} = \frac{V_{23}}{I_{14}}$$

and according to [29] to the sheet resistivity

$$\rho_S = \frac{\pi t}{ln(2)} \cdot \frac{R_{12,34} + R_{23,14}}{2} \cdot f \tag{2.13}$$

where t is the thin film thickness and f is a correction factor. This factor is only depending on the ratio of determined values for $R_{12,34}$ and $R_{23,14}$ and can be used as a measure for homogeneity of the thin film material.

2.4.3.2 Cyclic voltametry (CV)

Cyclic voltametry (CV) is a potential sweep method based on a three-electrode setup including working-, counter- and reference-electrode in combination with a potentiostat (figure 2.7 (a)) to study redox systems regarding to their potentials and electrochemical reaction rates. For this purpose a potential, applied to the working electrode i.e. the catalytic thin film, is ramped linearly while the scan direction is changed at a defined switching potential E_λ. The resulting potential is given either by equation 2.14 for $0 < t \leq \lambda$ or by 2.15 for $t > \lambda$ [30]

$$E = E_i - \nu \cdot t \tag{2.14}$$

$$E = E_i - 2\nu \cdot \lambda + \nu \cdot t \tag{2.15}$$

where E_i is the initial potential, ν is the scan rate and λ is the switching time. Reaction constants k_{red} and k_{ox} of a heterogenous charge-transfer reaction $\mathrm{O} + \mathrm{e}^- \underset{\mathrm{k_{red}}}{\overset{\mathrm{k_{ox}}}{\rightleftharpoons}} \mathrm{R}$ between an electrode and an analyte in solution are depending on the difference between electrode- and solution-potential. By variation of the electrode potential the reaction is driven far from equilibrium where either reduction ($E < E_{eq}$) or oxidation ($E > E_{eq}$) is enforced. Here, the resulting current is proportional to the reaction rate and by this enables the analysis of reaction kinetics [31, 32]. The current resulting from charge transfer at the working electrodes surface is determined between working electrode and counter electrode, while the potential is measured between working- and reference electrode. The method is not only suitable for the characterization of redoxactive analytes, but also for investigation of working electrode characteristics based on a specific reaction.

2.4.3.3 Electrochemical Impedance Spectroscopy (EIS)

Since cyclovoltametric measurements are affected by different parameters which are not related to the catalytic process, a data-correction is necessary to ensure the applicability of the method for characterizing solely the catalytic performance of the thin film material. In order to determine the different contributions to the measurement the total cell impedance is analyzed as a function of AC voltage frequency ω using electrochemical impedance spectroscopy (EIS). By this technique the different contributions to the total impedance, namely faradaic impedance due to the series resistance of an equivalent circuit R_S and pseudocapacity C_S as well as non-faradaic contributions namely solution resistance R_Ω and double layer capacitance C_d can be distinguished. The two latter ones are not characteristic for the material of interest, but are only related to the design of the electrochemcial cell. The concept of EIS is based on the analysis of the total impedance's frequency dependence during variation of an applied AC voltage and subsequent extraction of the different contributions from the resulting relationship, as described below.

For the following simplified approach two general contributions to the total impedance can distinguished. On the one hand charge-transfer resistance R_{ct} and on the other hand Warburg impedance Z_W, which can be considered as mass-transfer resistance R_W. The latter can be described as a serial circuit of a resistance, $R_W = \sigma\omega^{\frac{1}{2}}$, and the pseudocapacitance

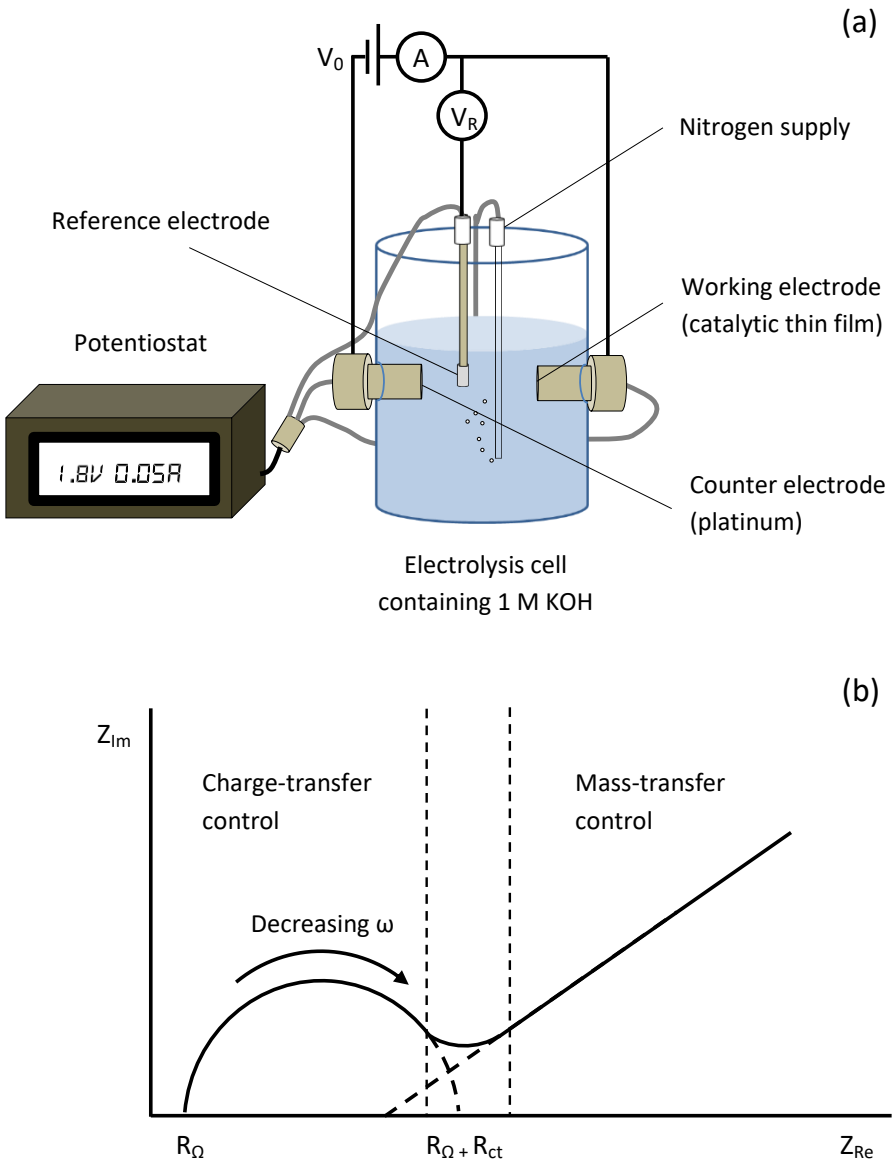

Figure 2.7: (a) Schematic sketch of an electrolysis cell for electrochemical characterization methods and (b) schematic Nyquist-plot for an electrochemical system.

$C_W = C_S = {}^{1}/_{\sigma \cdot \omega^{\frac{1}{2}}}$, where σ is a measure of concentration of a redoxactive reactant. The total impedance Z of the cell can be described as a series combination of the series equivalent resistance R_B and the series equivalent capacitance C_B of the cell which can be expressed as the real $Z_{Re} = R_B$ and imaginary $Z_{Im} = {}^{1}/_{\omega \cdot C_B}$ components of the total impedance.

Figure 2.7 (b) shows the schematic sketch of a Nyquist plot (Z_{Re} vs. Z_{Im}) obtained from EIS measurements.

Two regions dominated by charge-transfer at high frequencies and by mass-transfer at low frequencies as well as a transfer region can be distinguished. According to the literature Z_{Re} and Z_{Im} are described by the following equations 2.16 and 2.17, when the frequency range approaches zero ($\omega \to 0$).

$$Z_{Re} = R_\Omega + R_{ct} + \sigma \cdot \omega^{-\frac{1}{2}} \tag{2.16}$$

$$Z_{Im} = \sigma\omega^{-1}/2 + 2\sigma^2 C_d \tag{2.17}$$

These equations can be transformed to

$$Z_{Im} = Z_{Re} - R_\Omega - R_{ct} + 2\sigma^2 C_d \tag{2.18}$$

giving a linear relationship between Z_{Re} and Z_{Im} as reflected in the low frequency range of figure 2.7 (b). From equations 2.16 and 2.17 one can see that frequency dependence under these conditions only arises from Warburg impedance. Hence the observed linear relationship is characteristic for electrode processes controlled by means of mass-transfer.

With higher frequencies Warburg impedance increasingly loses significance and the charge-transfer resistance starts to dominate the process. Real and imaginary components for impedance of the resulting equivalent circuit ($\omega \to \infty$) are given by equations 2.19 and 2.20

$$Z_{Re} = R_\Omega + \frac{R_{ct}}{1 + \omega^2 \cdot C_d^2 \cdot R_{ct}^2} \tag{2.19}$$

$$Z_{Im} = \frac{\omega \cdot C_d \cdot R_{ct}^2}{1 + \omega^2 \cdot C_d^2 \cdot R_{ct}^2} \tag{2.20}$$

and after transformation equation 2.21,

$$\left(Z_{Re} - R_\Omega - \frac{R_{ct}}{2}\right)^2 + Z_{Im}^2 = \left(\frac{R_{ct}}{2}\right)^2 \tag{2.21}$$

describing a circular plot. This relationship is dominated by the capacitance of the double layer C_d. By reference to equation 2.19 and 2.20 one can see that the impact of this capacitance is strongly decreasing with increasing frequencies until solely ohmic resistance determines the process. In contrast low frequencies lead to a high impedance of capacitance and current flow is ruled by charge-transfer and ohmic resistance [30].

The correction of CV-data in accordance with equation 2.22 after determining the total ohmic serial resistance R_Ω from the high-frequency intersect with the real axis in the Nyquist-plot [7].

$$E_{iR-corrected} = E - I \cdot R_\Omega \tag{2.22}$$

2.4.4 Stoichiometric and chemical state characterization

2.4.4.1 X-ray photoelectron spectroscopy (XPS)

X-ray photoelectron spectroscopy (XPS) or electron spectroscopy for chemical analysis (ESCA) is a well established technique for surface sensitive analysis of various materials based on the photoionization of elements using x-rays of defined energies (see figure 2.8 (b)) and subsequent kinetic energy detection of the generated photoelectrons. It enables the investigation of core- as well as valence-electron energy levels and by reference to the resulting binding energies both, qualification and quantification of the involved elements. With respect to small shifts in the exact binding energies for pure elements ascribed to the chemical environment of the electron emitting atom, the method delivers information about bonding states and consequently about present chemical compounds. The average information depth is 50 Å. Due to the fact the information depth is related to the emission angle of photoelectrons, non-destructive depth profiling of the uppermost sample surface is possible by angle-resolved XPS measurements. The binding energy of the photoelectron E_{BE} is given by equation 2.23

$$E_{BE} = h \cdot \nu - E_{kin} - \Phi_A \tag{2.23}$$

where h is Planck constant, ν is frequency of the x-ray photon, E_{kin} is the kinetic energy of the photoelectron and Φ_A is the work function of the analyzer [33].

The principle of electron excitation and schematic design of x-ray photoelectron spectroscope is shown in figure 2.8 (a). Focused, monochromatic x-rays are generated by scanning an aluminum anode with a focused electron beam and the subsequent diffraction of the resulting radiation consisting of characteristic x-rays and bremsstrahlung. For that purpose an ellipsoidal quartz crystal is mounted in a 200 mm Rowland circle to select a narrow emission line for photoelectron excitation. By scanning the electron beam across the anode the resulting x-ray beam is scanned analogously across the sample surface.

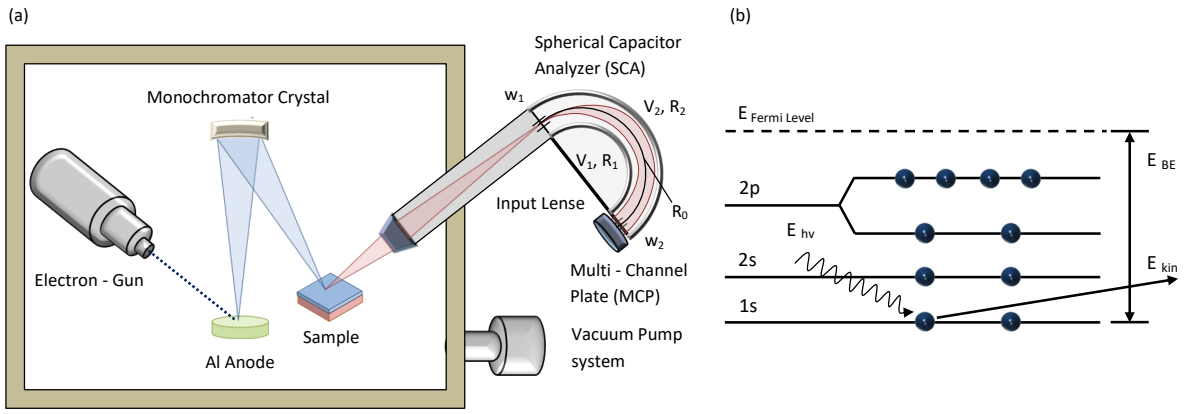

Figure 2.8: (a) Schematic sketch of a x-ray photoelectron spectroscope and (b) illustration of photoionization.

A spherical capacitor analyzer (SCA), consisting of an input lens, two concentric hemispherical electrodes and a multi-channel plate (MCP), enables the analysis of the photoelectron kinetic energies. Here a potential difference between the two hemispherical electrodes with potentials V_1 and V_2 and radii R_1 and R_2 forces the photoelectrons on almost circular trajectories, focusing them on the exit slit, followed by the MCP. In between the electrodes an equipotential plane is formed, connecting the entrance and exit slits of widths w_1 and w_2 of the analyzer. Equation 2.24 gives the condition for an electron of defined kinetic energy to pass the analyzer depending on the pass energy E_0, the range of possible entrance angles α_{max} due to the finite slit width and the electrode radii [34].

$$\Delta E = E_0 \cdot \left(\frac{w_1}{R_1 + R_2} + \frac{\alpha_{max}^2}{4} \right) \tag{2.24}$$

By variation of a deceleration voltage electrons of different kinetic energies are sequentially analyzed, while pass energy controls energy resolution and sensitivity.

As mentioned above the chemical shift in photoelectron energy relative to the photoelectron energy of the pure element is characteristic for the electronic and chemical states of an analyte and by that for specific compounds. This chemical shift is mainly depending on the electron-density present during the photoionization process. Due to charge transfer resulting from a chemical bond the effective charge of an atom becomes more positive having a binding partner of higher electronegativity leading to an increase of Coulomb attraction and hence an increase of binding energy. Analogous binding to an atom of lower electronegativity will cause a decrease in binding energy. In the same way nearest neighbours of an analyte influence the binding energy due to their different electronegativity and consequently varying electron-withdrawing character.

Depending on the electronic structure of the analyte the photoelectron spectrum can exhibit several features, for instance Auger electron peaks, spin-orbit splitting, multiplet splitting, shake-up peaks or plasmon loss peaks leading to superposition in peak areas and hampering the spectrum interpretation [33]. The latter three phenomena are frequently summerized and referred to as satellite structure. Here initial state effects related to the electronic environment before the photoelectron is emitted and final state effects can be distinguished. The latter can be of importance if the rearrangement of the analytes electronic structure due to the generation of a core-hole is sufficiently fast, so that the binding energy of the photoelectron is changed during the emission [35].

Table 2.1: Spin-orbit splitting intensity ratios [33].

Orbital	j values	Intensity ratio (peak area)
s	$^1/_2$	–
p	$^1/_2$, $^3/_2$	1 : 2
d	$^3/_2$, $^5/_2$	2 : 3
f	$^5/_2$, $^7/_2$	3 : 4

For instance spin-orbit splitting is an initial state effect. For all orbitals except s-levels, spin-orbit coupling will lead to a doublet with two electronic states and by this two separated peaks in the photoelectron spectrum. These doublets are due to the interaction between the magnetic moment arising from the electrons' spin and the magnetic moment from the orbitals angular

momentum. Here the intensity of the coupling and its effect on the difference in the electronic energy levels depends on the relative orientation of spin which is either parallel or antiparallel to the orbital magnetic moment [36]. The intensity of spin-orbit spitting increases for the same orbit with the atomic number Z and decreases with principal quantum number n, as well as for decreasing angular quantum number l at constant n. Due to the fact the doublet peaks reflect the degeneracy of the initial states, their relative intensity is defined for the different orbitals as shown in table 2.1.

On the contrary, multiplet splitting, as well as plasmon loss and shake-up peaks are final state effects. Shake-up peaks arise from excitation of an ion due to energy transfer from the photoelectron, leaving electrons in an excited state. Alternatively, they can occur due to emission of multiple electrons excited by the same photon. Plasmon loss peaks however arise from energy loss of the photoelectron by excitation of collective electron oscillation in the bulk or in surface layers of the sample [33]. Both phenomena result in photoelectrons with diminished kinetic energies and consequently lead to peaks at higher binding energies relative to the main peak.

Multiplet splitting can occur for atoms with unpaired electrons. After photoionization, the remaining unpaired core-electron interacts with the unpaired electron in the other orbitals causing several final states and consequently multiple peaks in the photoelectron spectrum. Also Auger electron emission is a final state process and results from the rearrangement of the electronic structure. The photoionization process produces n core-hole which will be occupied by electrons of higher-energetic orbitals. In that process energy is released as a x-ray photon. The subsequent energy transfer to an electron of an outer shell may cause the emission of an Auger electron. X-ray fluorescence and Auger emission are competitive processes, where x-ray fluorescence is dominating for elements with high atomic numbers and Auger emission for elements with low atomic numbers. However, several of these features can be used as additional characteristics to evaluate the XPS data, if a sufficient knowledge about the analyzed system is given.

2.4.4.2 Inductive-coupled-plasma mass-spectrometry (ICP-MS)

ICP-MS analysis is based on the ionization of analytes within a plasma and the subsequent separation of the resulting ions depending on their mass-to-charge ratio. The principle design of a mass spectrometer with inductively coupled plasma ionisation unit is illustrated in figure **??** with nebulizer, plasma torch, interface system, collision cell and quadrupole mass separator as main components.

The argon plasma is generated in a plasma torch consisting of three concentric quartz tubes, where different argon gas flows provide sample transport, plasma gas supply as well as cooling of the instrument. After the initial ionization using n Tesla unit the plasma is generated by beans of a high frequency induction coil.

The liquid sample is nebulized using argon gas to form an aerosol and transferred to the torch by argon carrier gas where sample components are decomposed, atomized and ionzed due to collisions with high energetic electrons and ions of the plasma. The plasma torch is in axial

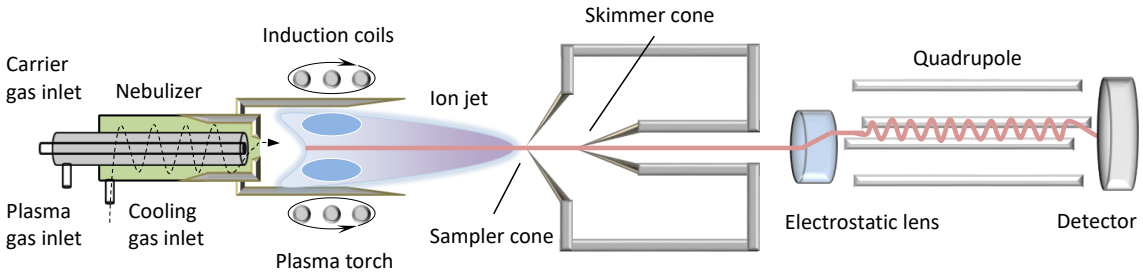

Figure 2.9: Schematic design of an mass spectrometer with inductely coupled plasma ionization unit,

orientation to the interface system consisting of a low vacuum and high vacuum region separated by a sampler and skimmer cone. Before entering the mass separator neutral species filtered by deflection of the ions using electrostatic lenses.

By means of a quadrupole mass separator, consisting of four ideally hyperbolic shaped, parallel rods, ions are forced on specific mass depending trajectories. By applying a positive as well as a negative potential at the opposing rods and superimposing additional radio frequency AC potentials, with a phase shift of 180 degrees to each other, ions are alternately focused and defocused. The quadrupole potential is described by equation 2.25

$$\Phi(\vec{r},t) = (U + V \cdot cos(\omega \cdot t)) \cdot \frac{x^2 - y^2}{r_0^2} \tag{2.25}$$

where U is DC voltage, V is the amplitude of AC voltage, r_0 is the radius surrounded by the hyperbolic rods, ω is the frequency of the AC voltage and x as well as y denote the directions of ion oscillation, passing the quadrupole in z-direction. By scanning the frequency or by variation of the applied potentials, ions of different mass-to-charge ratios are sequentially forced on stable trajectories.

3 Experimental section

3.1 Thin film fabrication

Substrate preparation

$La_{0.6}Sr_{0.4}CoO_3$ thin films with a thickness of t=100 nm were deposited on one-side epipolished single crystalline $NdGaO_3$ substrates in (001) surface orientation by PLD. NGO substrates, scaling 10 mm x 10 mm x 0.5 mm, were supplied by *Crystec GmbH, Berlin, Germany*. Initially the substrates were checked for contaminations by AFM as described below, to ensure clean surfaces. If required for parameter studies the substrates were divided into 5 mm x 5 mm x 0.5 mm pieces using a diamond cutter. Afterwards the pristine substrates were annealed in air for two hours at $T = 1000$ °C, including heating with a ramp for 90 minutes. Finally the substrates were scanned again by AFM to validate the quality of surface structure.

Pre-deposition

For the present study a PLD set-up (*Twente Solid State Technology (TSST),B.V., The Netherlands*) powered by a nanosecond KrF-excimer laser (*Lambda Physik Lasertechnik, Göttingen, Germany*) with a wavelength of $\lambda = 248$ nm was used. In-situ monitoring of the growth process was based on reflection high-energy electron diffraction.

After cleaning the heater using sandpaper, the substrates were fixed in the center of the heating platform. For this purpose the heating support was covered with a small amount of conductive silver paste (*Plano GmbH, Wetzlar, Germany*). The substrates were pressed into the silver paste to ensure good contact between the interface. Subsequently a heating voltage was applied for $t_1 = 15$ min at around $U = 10$ V, $I = 0.7$ A and $t_2 = 15$ min at around $U = 15$ V, $I = 1$ A. Also the $La_{0.6}Sr_{0.4}CoO_3$ ceramic target, supplied by *FZ Juelich Institute of Energy and Climate Research - Materials Synthesis and Processing (IEK 1)*, was burnished using sandpaper to remove ablation tracks caused by the previous PLD process and to obtain a smooth surface. The target was mounted on the target carousel in a defined position using a distance meter and installed within the main chamber via the load lock followed by the heater.

After adjusting heater and target parallel to each other in deposition position, target spinning was turned on and the required temperature was set. Oxygen pressure was aligned using a mass flow control (*Brooks Instrument GmbH, Hatfield, USA*) and a valve capable of variable positioning by means of a stepping motor (*Nanotec, Electronic GmbH & Co. KG, Munich, Germany*). Thereby a constant oxygen pressure is maintained in combination of the constant workflow of a turbo vacuum pump. The laser fluence was adjusted by varying the angle of a beamsplitter

relative to the incident laser radiation, while the gauging head of an energy measurement tool (*RBM - R. Braumann GmbH, Munich, Germany*) was positioned in the optical path. Final cleaning of the target surface was done by pre-ablation inside the PLD chamber, using a defined number of $N = 1200$ pulses with the respective laser fluence applied for deposition, while a shutter is placed in front of the substrate to avoid deposition.

RHEED

Before starting the deposition, the RHEED system was aligned, setting acceleration voltage to $V = 25$ keV and a emission current of $I = 1.4$ A. The position of primary electron beam was adjusted both, mechanically and by usage of a deflection unit. The mechanical adjustment involved positioning of the electron gun by a x-y-system as well as positioning of tilt angle and azimuth of the heating support relative to the electron beam. Once a clear diffraction pattern is displayed on the phosphor screen, regions for the monitoring of intensity oscillation were defined.

Deposition parameters

After starting the video- and oscillation- record the deposition was started. The deposition typically was performed at an oxygen pressure of $p(O_2) = 0.053$ mbar, a substrate temperature of $T = 650$ °C at repetition rates of $f = 5$ Hz. The laser fluence was varied between 1.31 J·cm^{-2} and 2.62 J·cm^{-2}. The target-to-substrate distance was x = 60 mm. The deposition time was calculated using the initial RHEED oscillation period, reflecting the growth of one unit cell, based on the simplified assumption of unit cells scaling $a = 4$ Å. Considering the difference in thermal expansion coefficients of the materials (see section 2.1) the heater was slowly cooled down with $T = 10$ °C per minute at deposition conditions to avoid cracking of the thin film during cooling. A picture of the RHEED pattern was taken before and after the deposition respectively. The deposition parameters were chosen, in reference to [37].

3.2 Thin film characterization

After cooling down the system, the thin films were removed from the heating support and characterized as follows.

AFM

Initially the thin films were scanned by AFM (*Oxford Instruments Asylum Research Inc., Santa Babara, USA*) with AC-mode imaging. For this purpose the sample was placed on the rigid x-y-z-stage and the height was roughly adjusted. After the laser spot position was centered on the backside near to the end of the cantilever, the objective lens of the optical microscope was adjusted in order to bring the end of cantilever in focus. Subsequently the sample focus point was adjusted and set to the required height. By moving to the pre-engage position, the tip-to-surface distance was automatically reduced, based on the tip and sample positions adjusted in the previous steps.

To determine the resonance frequency of the cantilever, the frequency of the piezoelectric element was tuned over a defined range between f = 50 - 400 kHz while monitoring the resulting change of amplitude and phase. The operating frequency is chosen with an small offset (- 5 %) relative to the resonant peak. This offset was adjusted to the low-frequency side, considering the frequency shift due to the tip approach towards the sample and ensuring a tip distance in repulsive mode. Eventually the tip is automatically aligned around three microns off the surface by an alternating process of tip-approach with respect to the set point amplitude and the scanning process was started. Typical an area of 5 m^2 was scanned over a number of 512 points and lines with scan-rate of 1.45 Hz.

XRD

Crystallographic analysis was done by x-ray diffraction measurements. Here, scans in $2\Theta/\Theta$ geometry with a *D8 Advance* diffractometer (*Bruker, Massachusetts, USA*) were performed using a Cu K_α x-ray tube with the wavelength $\lambda_{K_{\alpha,1}} = 0.1540598$ nm. Reciprocal space mapping was performed with a *PW 3020 X'Pert Diffractometer* (*PANanlytical, The Netherlands*) using an optical system providing the $\lambda_{K_{\alpha,1}} = 0.1540598$ nm and $\lambda_{K_{\alpha,2}} = 0.15444426$ nm. To ensure good quality measurements, several calibration steps were done previous to the analysis of each sample. First of all, relative detector-to-x-ray-tube-position was aligned. Furthermore alternating calibration of the sample stage position in z-direction and of the sample tilt was done to bring the sample in the middle of the beam path and align the sample height. To achieve high precision, the signal was initially adjusted to define zero value, followed by the adjustment to the intense (002) substrate peak for $2\Theta/\Theta$- or (013) substrate peak for RSM-scans.

Electrical characterization

For electrical characterization the LSCO thin films were contacted to 10 mm solder pad sample cards by ultrasonic Al-wire bonding (*Kulicke & Soffa Industries Inc., Singapore*) Subsequently the contacts were checked using a multimeter (*Beckmann Components GmbH, Munich, Germany*) before four-point-probe resistivity measurements were performed at room temperature using an AC/DC Hall Effect Measurement System Model 8404 (*Lake Shore Cryotronics Inc., Ohio, USA*). For the measurement in the standard resistance mode reasonable excitation currents, leading to sufficient voltages for precise measurements ($V \geq$ 1 mV), were applied. However the current has to be low enough to not heat or damage the thin film or exceed the linear voltage-range. To assure a linear correlation and by this good quality contacts, an ohmic check was performed between contacts 1 and 3 as well as 2 and 4 previous to all measurements. Plotting voltage vs. several currents applied in the range around the final measurement the linearity was observed. The average resistance was calculated over ten measurements respectively. Typically, tesistivity measurements were performed with excitation currents of $I = 5$ μA.

Stoichiometric characterization

For analysis of stoichiometry in the near-surface region, XPS measurements were performed with a *Phi 5000 VersaProbe* system (*ULVAC Phi, Physical Electronics Inc., USA*) using the Al $K_{\alpha,1}$ line (E_λ=1486.6 eV, FWHM=0.26 eV) of a monochromized x-ray-source. After mounting the samples onto the support, they were installed within the main chamber via load lock and sample positions were defined. After adjustment of sample height with respect to the maximum intensity for the O 1s signal, binding energy ranges as well as lateral positions and angles for the measurements were set. Besides a full energy range survey and O 1s-, Co 2p-, Sr 3d- and La 3d-core-level spectra were analyzed with take-off angles of $\Theta_1 = 26$ degrees and $\Theta_2 = 76$ degrees respectively. For all measurements pass energy was kept constant at $E_0 = 29.35$ eV for high energy resolution analysis in fixed analyzer transmission mode (FAT).

Furthermore the target material was analyzed analogously for the purpose of calibrating the relative sensitivity factors (RSF) of the system to the material of known composition. XPS data was fitted with Casa XPS Commercial Software by using a mixed Gaussian-Lorentzian peak shape (GL 30) after a Shirley-type background was subtracted and an energy calibration to the O 1s perovskite peak was done. All fittings were performed after calibrating the binding energies of the spectra to the perovskite lattice oxygen peak. For this defined relative peak positions and constant FWHM were assumed within a scope of $\Delta_{BE} = 0.2$ eV and $\Delta_{FWHM} = 0.2$ to make concessions to measurement uncertainties. The fitting of signals for strontium, resulting from spin orbit splitting were fitted with defined intensity ratios (see table 2.1) and equal FWHM in conformity with the degeneracy of the electronic levels. The quantification was performed by using the fitted peak areas. For the quantification of oxygen of pristine thin films, the hydroxide peak, varying strongly with cleaning procedure and consequently with contaminations was neglected.

For analysis of the bulk stoichiometry, ICP-MS analysis of Co, La and Sr was realized by *FZ Juelich, Central Institute of Analytics* (*ZEA-3*). For this purpose the thin films were dissolved in a mixture of $V = 4$ ml hydrochloric acid and $V = 1$ ml hydrogen peroxide. Afterwards the solutions were diluted to a total volume of $V = 25$ ml before three aliquot parts of the solutions were analyzed per sample (Agilent 7500ce, USA). Additionally a NGO substrate was analyzed as reference material after analogue treatment. The quantification was performed by means of an four-point calibration in the range between $c = 5$ - 50 μg·l for each element. Rhodium was used as internal standard. The samples were scaled before and after the dissolution.

Electrochemical characterization

For the following catalysis experiments contact pads scaling 8 mm x 0.5 mm were sputtered on surface adjacent to the four edges of the thin films to ensure good contact to the potentiostat during electrolysis. Platinum layers with a thickness of $t = 50$ nm were deposited using a sputter mask which was manufactured for this purpose. Electrochemical experiments were performed in a self-constructed electrolysis cell with the ability to use thin film electrodes provided by Daniel Bick (*IWE 2, RWTH Aachen University*). Additional titanium layers between thin film material and platinum pads for the purpose of a better adhesion of platinum contacts emerged as hampering the electrolysis process.

In order to use the thin films as working electrodes within the electrolysis cell, they were mounted onto an electrode supply as shown in figure 3.1. For fixing the samples at the electrode supply a glass-ceramic sample holder scaling 25 mm x 25 mm with a sample-scaled recess in its center was produced. For bonding, two edges of the sample holder were taped with adhesive copper strips respectively, reaching up to the edge of the recess. Soldering the two ends of a converging cable to the copper foil strips at the back of the sample holder provides the contact to the potentiostat. After the sample-holder construction was put in the recess on top of the electrode supply with the cable inside the hollow tube, the platinum contacts at the thin films surface were connected with the copper tape by soldering using indium as contact material. The screw cap of the electrode supply with a circular opening in its center was prepared by inserting an O-ring with an diameter of $r = 0.8$ cm. Afterwards it was screwed to the electrode supply until the O-ring was in contact to the thin film. Using this set-up a defined surface area of the thin film material, serving as working electrode was provided for electrocatalysis, while the rest of the construction, in particular the platinum contacts, were shielded from the electrolyte.

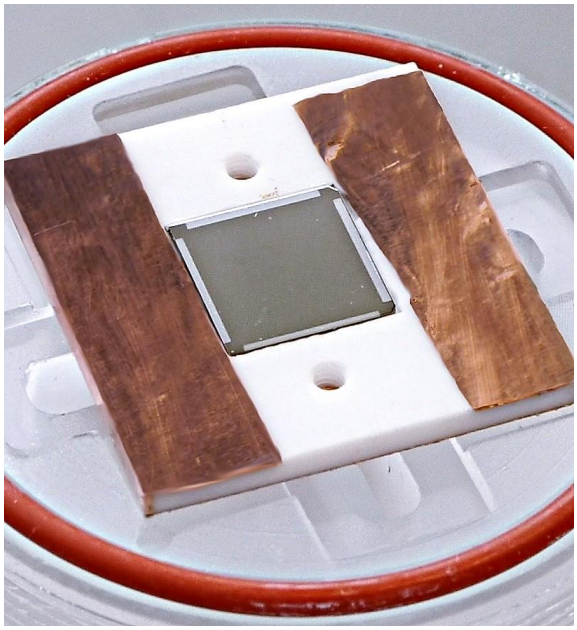

Figure 3.1: Image of a 10 mm x 10 mm LSCO thin film on NGO, inserted to the 25 mm x 25 mm glass-ceramic sample holder and placed on the electrode support. At the four edges of the thin film 10 x 10 mm platinum layers with a thickness of 50 nm can be seen. The construction is connected to the potentiostat by a cable, soldered to the copper foil on the back of the sample holder. In the next step, indium foil is used to connect copper foil and thin film and a screw-cap is adjusted at the sample, providing a defined circular area in the center of the thin film for the subsequent electrochemical experiments.

Before mounting the ready-to-use working electrode construction and the platinum counter electrode into the electrolysis cell, the contact between thin film surface to wire were checked using

a multimeter. The electrolysis cell as well as the Hg/HgO reference electrode (*Radiometer Analytical, USA*) were filled with 1 M potassium hydroxide solution prepared from KOH pellets (*Sigma Aldrich, USA*) using deionized water. After connecting the electrodes to the potentiostat (*Metrohm Autolab B.V., The Netherlands*) the electrochemical characterization was performed by measurement of the pre-analysis open circuit potential, electrochemical impedance spectroscopy, cyclic voltametry in dynamic state, post-analysis open circuit potential and subsequent quasi-stationary Tafel-measurement. EIS was carried out at frequencies between 1 Hz and 100 kHz. CV measurements were performed starting from the equilibrium state determined based on the open circuit potential with a cycling potential up to 2.1 V and a scan rate of 0.1 V per second. For all samples, multiple CV sweeps ($\sim$ 30) were performed. The analysis took place at room temperature in a still solution enabling the observation of both charge-transfer and diffusion and controlled processes. Between two measurements the electrolyte was purged with nitrogen gas to supply the electrodes surface with fresh reactants. The alkaline electrolyte provides high conductivity of the aqueous solution. After electrochemical experiments the thin film samples were removed from the electrode supply, cleaned with deionized water and dryed with compressed nitrogen.

Subsequent to the electrochemical measurement the thin film was analyzed following the same procedure as described above.

4 Results

This chapter deals with the characterization of growth and material properties of epitaxial LSCO thin films fabricated with various laser fluences in regard to their morphological, crystallographic, electrical and stoichiometric properties. Based on this studies, LSCO thin films deposited at optimized fluences are characterized with respect to their performance in catalysis of the oxygen evolution reaction. Furthermore a short insight to the degradation of the thin film material is given.

4.1 Growth of LSCO thin films on NGO

For the further study of material properties, cobaltite thin films of constant thicknesses of around 100 nm were deposited on NGO with varying laser fluences between 1.31 J·cm^{-2} and 2.62 J·cm^{-2} as one of the main parameters for the PLD process.

4.1.1 Substrate preparation

Since the as-received NGO substrates were epi-polished, they exhibit disordered surface morphologies as can be seen from figure 4.1 (a). By means of a high-temperature treatment, as described in section 3.1 a reconstruction of the surface to a single (001) orientation is achieved. Due to this annealing process NGO substrates with well-defined surface terrace structures and an average roughness of $RMS = 0.13$ nm were obtained. The resulting surface morphology after annealing of the substrate is illustrated in 4.1 (b). The terrace step height is in size of one unit cell, the terrace step width is typically of the order of a few hundred nanometers, but is varying depending on the miscut angle between crystal surface and crystal lattice plane resulting from the polishing process.

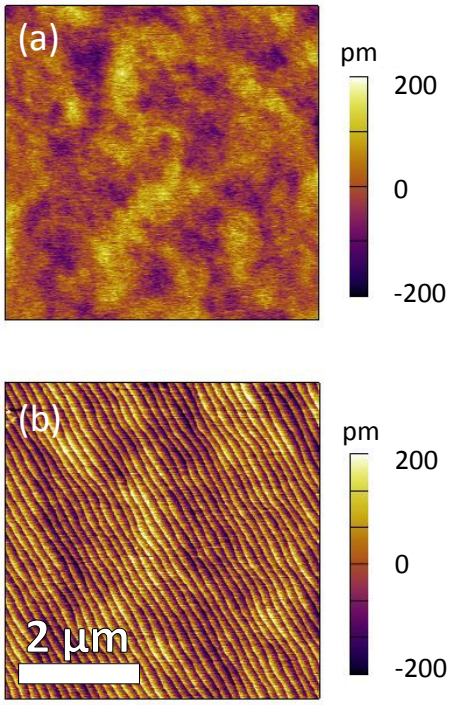

Figure 4.1: Surface morphologies of a (a) pristine and (b) annealed (001) NGO substrate. Images are in the size of 5 x 5 μm.

4.1.2 Investigation of growth kinetics

A detailed list of the parameters used for the PLD process can be found in section 3.1.

In figure 2.4 the evolution of the RHEED intensity (a) during deposition of 100 nm as well as (b) for the initial growth phase about first 20 nm are illustrated. Additionally RHEED patterns of the initial and final state of growth, related to the NGO substrate and LSCO thin film surface are shown (c). Furthermore a false colour picture of a superposition of both patterns is given.

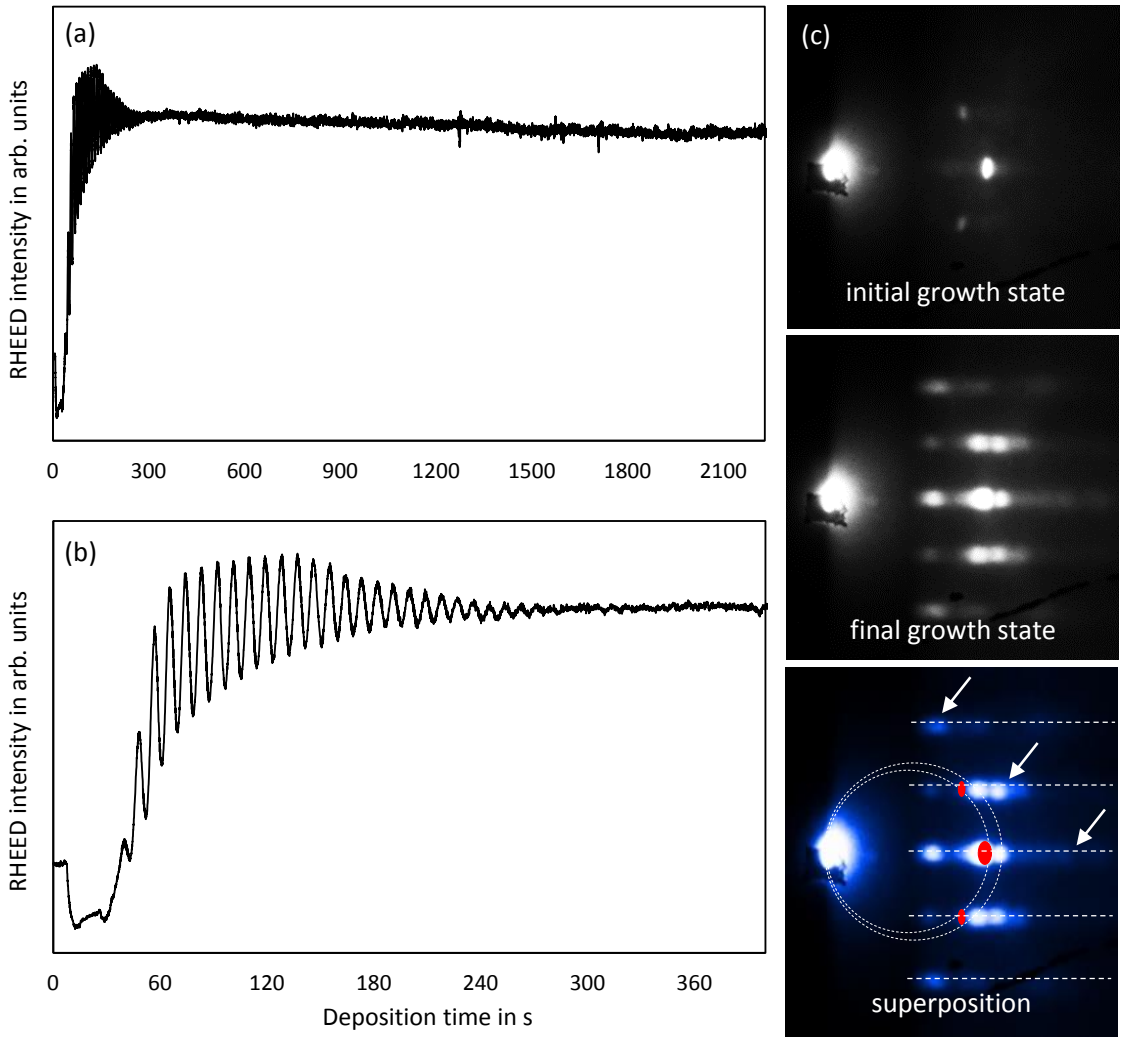

Figure 4.2: Representative RHEED intensity evolution during PLD growth of heteroepitaxial LSCO thin films exemplary shown for a laser fluence of 2.19 J·cm^{-2}. (a) for the growth of LSCO with a thickness of 100 nm, (b) initial growth phase of around 40 unit cells, and (c) corresponding diffraction pattern of the initial and final growth stage as well as a superimposed picture.

Subsequent to a loss in intensity at the moment of first deposition due to the initial roughening of the surface, a quick recovery of intensity followed by strong oscillations with growing intensities are observed as illustrated in 4.2 (b).

With increasing deposition time, the average intensity of the specular RHEED spot increases further, eventually saturating. After reaching a maximum in intensity, the attenuation of the

oscillations lead to a transition to an almost constant intensity level at a deposition time around t=300 s. Besides a slight reduction of intensity over time, no significant changes in RHEED intensity are monitored during the further deposition process (4.2 (a)). Small glitches within the intensity trend are probably due to vibrations of the detection unit. Table 4.1 shows the deposition rates for PLD-growth of LSCO films at various laser fluences calculated from RHEED intensity oscillations as described in section 3.1.

As shown in figure 4.2 (c) the RHEED patterns of the initial and final growth state exhibit significant differences. Apart from the large primary electron spot which is only partly blocked by the substrate at the left-hand side of the image, three smaller spots can be observed on the right-hand side of the initial pattern. As shown in the superimposed picture, all signals are located on a circle (Laue circle), where the sharp specular spot at the same height as the primary spot shows the highest intensity, while the diffraction spots below and above the specular spot are much less intense. Furthermore very weak horizontal streaks superimposing the spots can be observed.

In contrast to the initial state, the final state RHEED pattern is much more complex and exhibits several additional diffraction features. Besides significantly more distinct streak features, new diffraction spots as well as broadened and slightly displaced spots relative to the former pattern can be observed. Furthermore, both specular and diffraction spots gain in intensity as compared to the initial intensity. The false colour plot, where both RHEED patterns are superimposed and the initial-state RHEED pattern is illustrated in red and the final state pattern is illustrated in blue, enables an easy comparison of the spot positions. Here an increase in the circumference of the Laue-circle and the streak feature as well as some additional diffraction spots, denoted by dashed lines and white arrows respectively, are shown. The defined diffraction pattern observed even after the growth of 100 nm of LSCO indicates a well-defined crystal structure of the thin films surface and due to the grazing incidence of electrons in RHEED a rather smooth thin film surface, as will be discussed in more detail below.

Table 4.1: Deposition rates for PLD-growth of LSCO at various laser fluences obtained from RHEED anaylsis.

Laser fluence in J·cm^{-2}	Deposition rate in Å per pulse
1.31	0.059
1.53	0.066
1.75	0.070
1.97	0.077
2.19	0.082
2.41	0.085
2.62	0.097

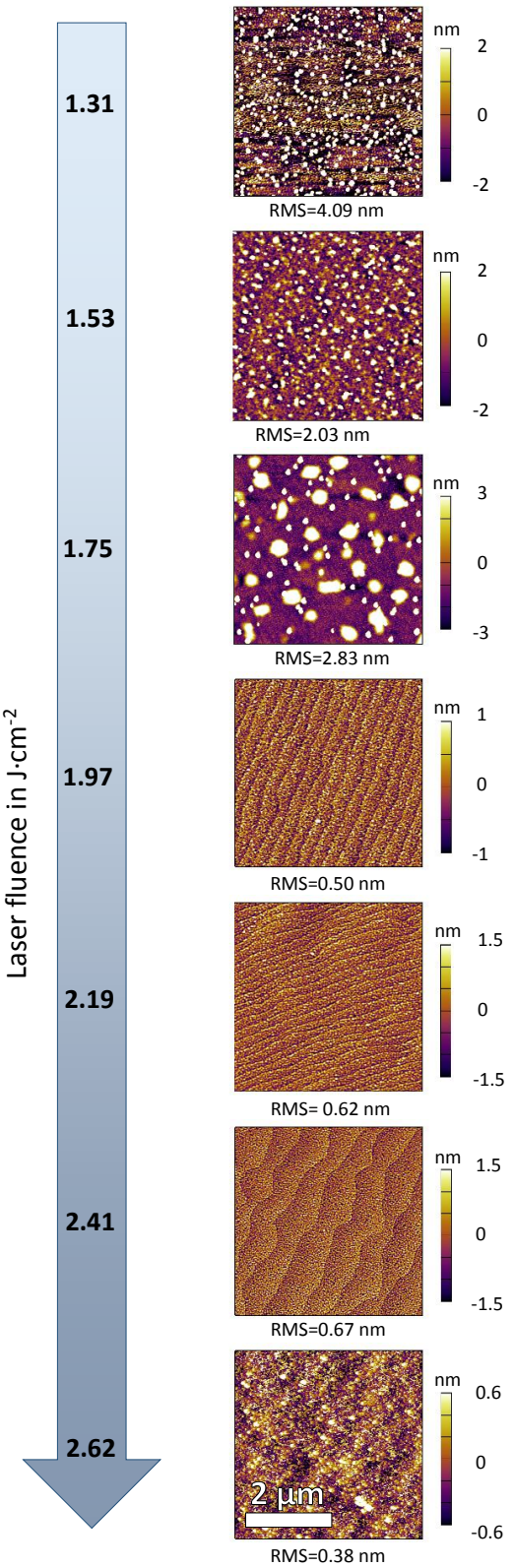

Figure 4.3: Surface morphologies and corresponding surface roughness of 100 nm thick heteroepitaxial LSCO thin films grown at different laser fluences (AFM scan-size 5 x 5 μm^2).

4.1.3 Crystallographic and morphologic characterization of LSCO thin films

As shown in figure 4.3, the surface morphology of the LSCO thin films is strongly depending on the laser fluence applied during deposition. Here, the AFM images as well as the corresponding surface roughness (RMS) is given for the respective laser fluence. For a comparison of the morphologies the particular color bar should be noted.

In general the film morphologies reflect a trend of decreasing surface roughness with increasing laser fluence. In the low-energy range, thin films exhibit similar morphologies with distinct features ranging from spherical to arbitrary shape and with varying sizes. Consequently these films exhibit a high surface roughness with RMS $<$ 4.1 nm relative to films grown at higher fluences.

A significant change in surface morphology is visible for films grown at laser fluences between 1.97 J·cm^{-2} and 2.41 J·cm^{-2}. In this medium energy films exhibit a clear step terrace structure with varying step width, depending on the substrates' terrace structure. Correspondingly thin films grown within this energy range exhibit a relatively low surface roughness. However, compared to the morphology of annealed substrates (fig. 4.1 (b)) small features, which can be recognized as grain texture on top of the terraces, remain on the surface causing a residual roughness below RMS $<$ 0.6 nm. At high laser fluences of 2.62 J·cm^{-2} roughness is decreasing further on, but no terrace step structure is visible. Here again, the surface exhibits an increased heterogeneity compared to films grown in the medium range.

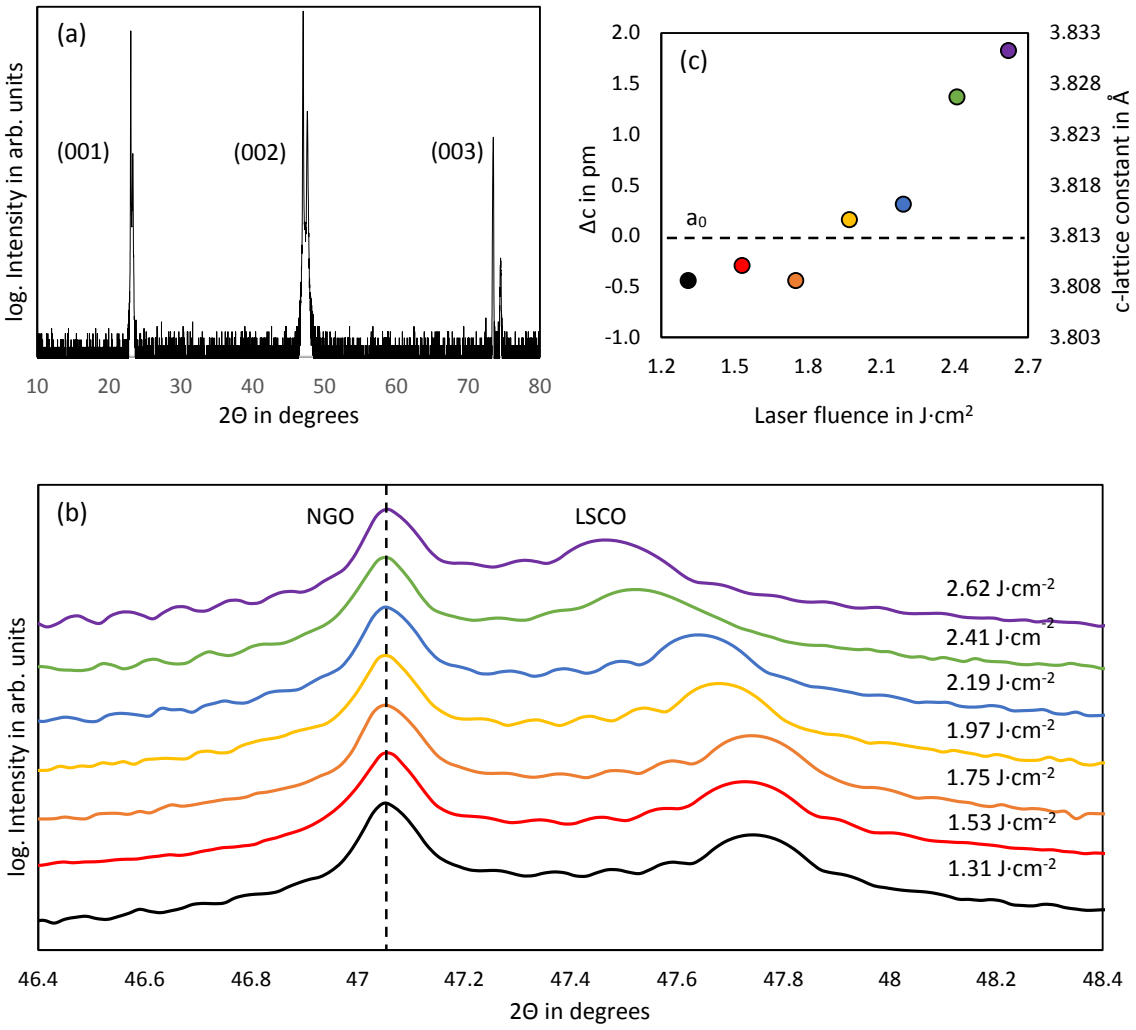

Figure 4.4: (a) Representative wide-angle x-ray diffractogram of a LSCO thin film with a thickness of around d=100 nm recorded in 2Θ/Θ-geometry. (b) diffractograms of 100 nm LSCO thin films grown at various laser fluences recorded in 2Θ/Θ-geometry around the (002) peak and (c) plot of corresponding shift in calculated c-lattice constants against laser fluence.

In figure 4.4 (a) the x-ray diffractogram of a LSCO thin film deposited on NGO, measured in 2Θ/Θ-geometry over the range of 2Θ = 10 - 80 degrees is shown in a logarithmic plot. Three pairs of peaks at angles about 2Θ = 23.53 degrees, 2Θ = 47.06 degrees and 2Θ = 70.59 degrees, with a signal at lower and a signal at higher diffraction angles, corresponding to a larger and smaller c-lattice constant can be seen. These double-peaks represent the (001), (002) and (003) diffraction peaks of the NGO substrate and LSCO thin film respectively. Due to the larger thickness, the substrate material shows sharp peaks with high intensities while the thin film gives rise to broader peaks of lower intensity. Reflection on crystallographic planes of larger distances and accordingly higher Miller indices lead to an increase in the magnitude of separation of the double-peaks with increasing 2Θ-angles. Apart from these double peaks, no further signals were detected indicating single phase epitaxial LSCO thin films.

With a closer look to the (002) peaks as shown in figure 4.4 (b) for LSCO films grown at different laser fluences, the difference in peak position, width and intensity gets more apparent. Further-

more clear thickness fringes can be observed for all films in the vicinity of the film peak. The (002) NGO substrate peak is observed at $2\Theta = 47.059$ degrees. The LSCO thin film peak is typically observed at angles between about $2\Theta \approx 47.5$ degrees and $2\Theta \approx 47.8$ degrees. Additionally a shift of the film peaks to lower 2Θ-values correlating with larger c-lattice parameters can be seen for laser fluence exceeding 1.75 J·cm^{-2}. With respect to the 2Θ-values, an increase in the c-lattice parameters of around $\Delta c \approx 2.3$ pm with increasing laser fluences can be observed. The theoretical bulk lattice parameter of LSCO is $a_0 = 3.813$ Å. For elucidation of this phenomena the relation between magnitude as well as relative change in c-lattice constant and laser fluence is illustrated in figure 4.4 (c) relative to the bulk reference lattice constant a_0. According to equation 2.12 the average film thickness estimated from first order thickness fringes is t=96.5 nm. Differences in manifestation of the oscillations are due to variations in scan time.

For a further examination of the thin film properties reciprocal space maps of the films were measured. In figure 4.6 the RSM, where in-plane versus out-of-plane lattice constants are plotted for the different samples, are shown. Analogous to the $2\Theta/\Theta$-measurements, two intensive signals, related to substrate and thin film material, can be observed for all applied laser fluences during growth. As expected, the signal for the thicker substrate is more intense than the signal for the thin film. The splitting of the signals in two areas of high intensity what especially can be observed for the intensive substrate signals is resulting from the specific setup used for RSM measurements providing two wavelengths (Cu $K_{\alpha,1}$ and Cu $K_{\alpha,2}$). Substrate and film signals have similar in-plane lattice constants, while a clear difference in the out-of-plane signal can be observed. The distance between the two signals reflect, similar to figure 4.4 (b) the difference in their out-of-plane lattice constant. Variation in intensity can be occur due to misalignment in z-position.

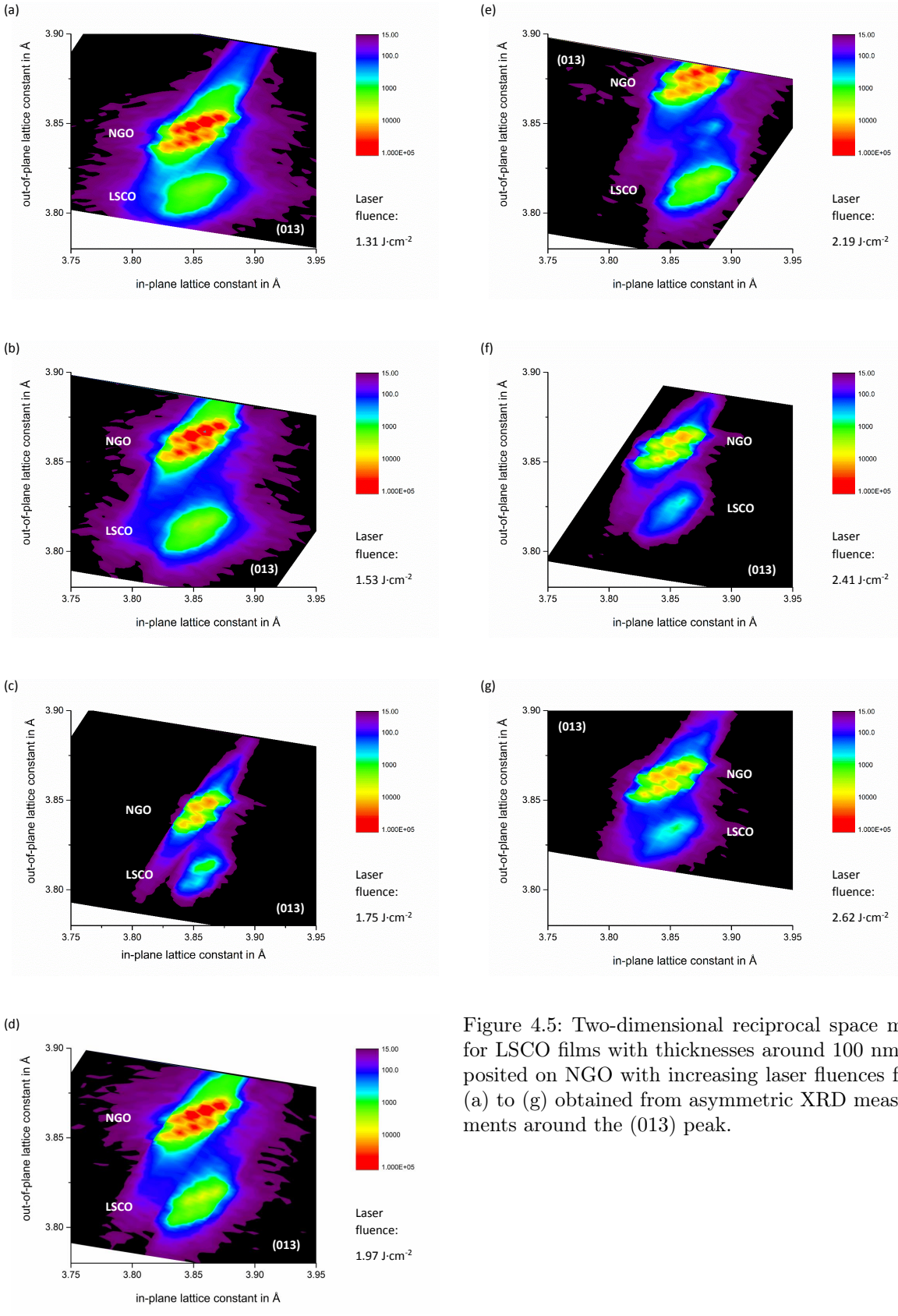

Figure 4.5: Two-dimensional reciprocal space maps for LSCO films with thicknesses around 100 nm deposited on NGO with increasing laser fluences from (a) to (g) obtained from asymmetric XRD measurements around the (013) peak.

4.1.4 Electrical characterization of LSCO thin films

Electrical properties of the thin films were determined at room temperature as one important parameter for electrocatalysts. The NGO substrate is highly insulating, thus avoid any leakage currents during electrical measurements. Based on four-point probe resistivity measurements, the sheet resistivity as well as corresponding F-value was determined as shown in 4.2. The average sheet resistivity of 100 nm LSCO thin films is ρ_S =25.4 $\Omega \cdot \square^{-1}$, which is extraordinarily low for complex oxides. The F-values vary in the range between F=0.95 to F=1.00.

Table 4.2: Mean values of sheet resistivity and corresponding F-value for LSCO thin films of around 100 nm on NGO substrates grown with various laser fluences obtained from four-point probe measurements.

Laser fluence in J·cm^{-2}	Sheet resistivity ρ_S in $\Omega \cdot \square^{-1}$	F-value
1.31	22.9	0.99
1.53	27.0	0.95
1.75	25.7	1.0
1.97	23.4	1.0
2.19	21.7	0.96
2.41	24.8	0.95
2.62	32.1	1.00

4.1.5 Stoichiometric and chemical state characterization of LSCO thin films

Stoichiometry was determined by means of ICP-MS analysis as well as angle-resolved photoelectron spectroscopy. While for bulk stoichiometry of the thin films, cobalt, lanthanum content and strontium were quantified after dissolving the samples as described in section 3.2, XPS provided information about the stoichiometry and chemical composition in the near-surface region. Here angle-resolved XPS enables depth profiling, where the surface sensitivity is increasing with decreasing take off angles. Furthermore the change in average cobalt valency relative to the target material was investigated, based on the deconvolution of the Co 2p spectrum.

In this section, first the deconvolution of the core level spectra into their respective components will be discussed and model fitting procedure will be illustrated. Subsequently, the resulting thin film stoichiometry for different laser fluences obtained from ICP-MS and XPS will be discussed.

In figure 4.6 representative XPS core-level spectra of LSCO thin films are illustrated, including the peaks obtained by deconvolution of the signals by curve fitting, reflecting different components of the observed elements.

As can bee seen from 4.6 the O 1s spectrum is dominated by one large peak, with a shoulder to the high-energy side. In accordance with the literature [38, 39] the O 1s spectrum was deconvoluted into three components. The signal at BE $\approx$ 528.6 eV was assigned to lattice oxygen while a second component at a higher binding energy (BE $\approx$ 529.8 eV) was assigned to oxygen of lower coordination at the termination layer [35]. The third high-energy component with BE $\approx$ 531.3 eV is associated with hydroxides and carbonates at the surface [40, 41].

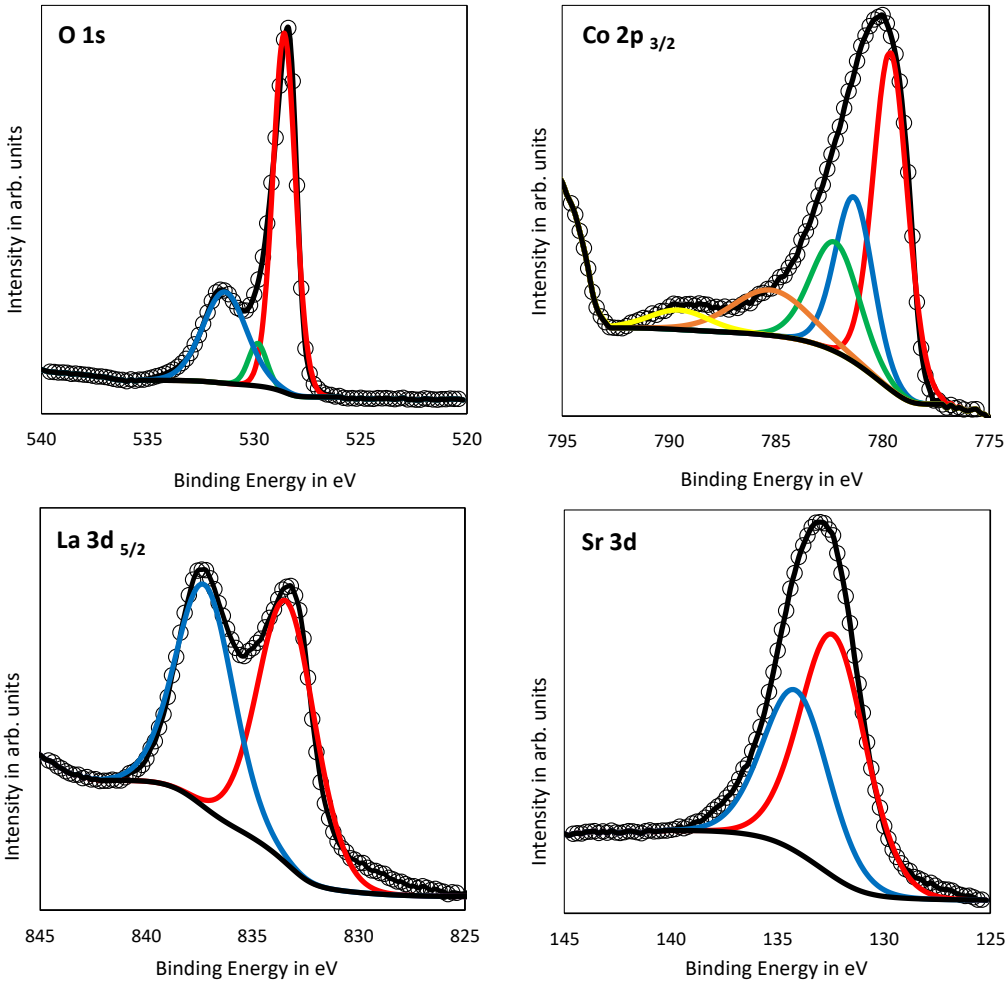

Figure 4.6: Representative O 1s, Co 2p, La 3d and Sr 3d core-level spectra for LSCO thin films obtained by photoelectron spectroscopy, where the black line highlighted by circular symbols indicate the original signal and the plain black line corresponds to the background. In the O 1s spectrum the perovskite component is shown in red, the component dedicated to the termination layer is shown in green and a hydroxide/carbonate peak is shown in blue. In the cobalt spectrum, here limited to the $2p_{3/2}$ signal, the trivalent cobalt is shown in red, the two peaks assigned to divalent cobalt are shown in blue and green and the satellite peaks are shown in orange and yellow respectively. In the La 3d spectrum two peaks related to the La $3d_{5/2}$ signal are shown in red and blue. In the strontium spectrum the overlapping $3d_{5/2}$- and $3d_{3/2}$-signals are shown in red and blue respectively.

The complex shape of the Co $2p_{3/2}$ spectrum with an asymmetric main peak is based on several superimposed signals. These are resulting from cobalt of different valency as well as multiplet splitting for divalent cobalt compounds and a significant satellite structure at higher binding energies relative to the main peak. Due to this complexity the interpretation of Co 2p photoelectron spectra remains to be highly discussed and often inconsistent in the literature. Based on extensive literature research a model for deconvolution of the various signals was developed.

With respect to the valency of cobalt, the Co 2p spectrum gives fundamental information about the nature of cobalt bonds. As shown for several transition metals, the effective ionic charges differ from expectations based on formal oxidation states and the principle of charge neutrality. Due to the impact of charge transfer effects between cobalt and oxygen in the Co-O bond, true ionic charges of cobalt usually are much less than predicted from formal oxidation states [42]. Consequently the Co 2p spectrum qualitatively does not differ significantly from other cobalt compounds of mixed valency such as Co_3O_4 [43] and an approach using the fitting parameters obtained from deconvolution of Co_3O_4 spectra was applied.

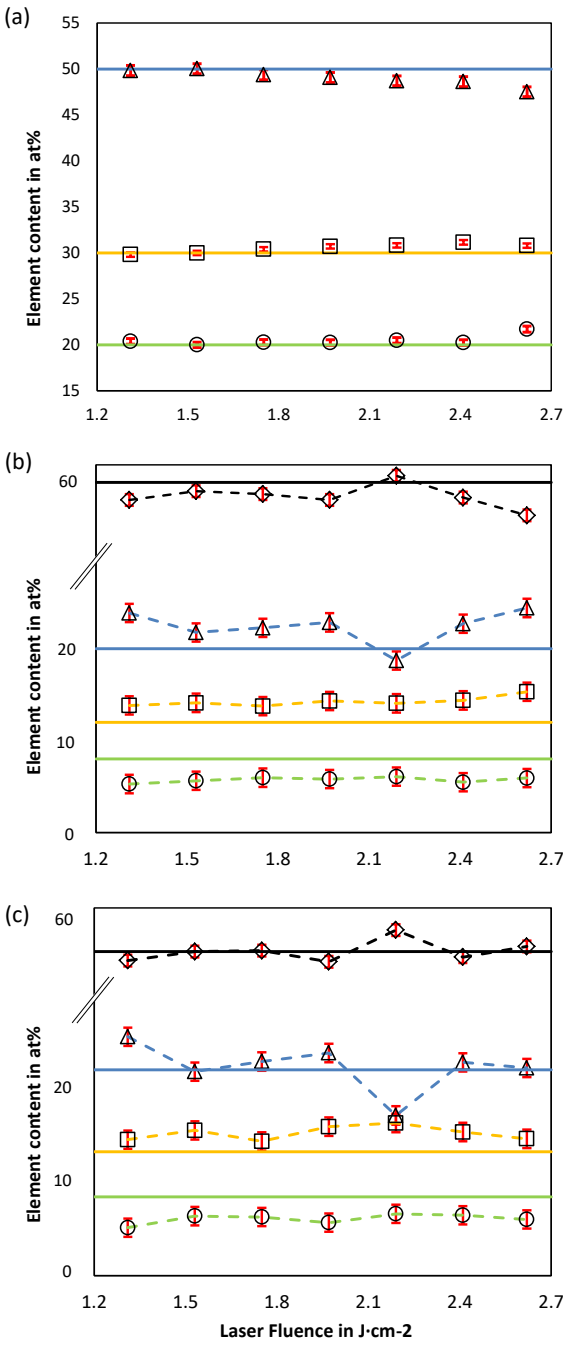

Figure 4.7: Elemental composition of LSCO thin films grown at various laser fluences, obtained from (a) ICP-MS and XPS analysis at take-off angles of (b) 26 degrees and (c) 76 degrees. Triangles and blue colour denote cobalt-, squares and yellow colour denote lanthanum-, circles green colour denote strontium and rhombic symbols as well as black colour denote oxygen-content. The different symbols describe measuring values, solid lines denote the ideal content of respective elements for the target material (for (c) measured values relative to (b)). Dashed lines are a guide for the eye. Error bars are given in red, overlayed to the symbols, where an constant error of 1 at% was assumed for XPS and errors for ICP-MS measurements are based on standard deviations obtained from multiple samples.

Five components, including trivalent cobalt at a binding energy of BE $\approx$ 779.6 eV and two peaks (ms1 and ms2) for divalent cobalt arising from multiplet splitting at BE $\approx$ 781.4 eV and BE $\approx$782.3 eV respectively, can be distinguished. Two satellite peaks at BE $\approx$ 785.3 eV and BE $\approx$ 789.6 eV give rise to a distinct satellite structure at higher binding energies relative to the

main peak. Curve fitting of the Co $2p_{3/2}$ photoelectron spectrum was performed with respect to the comprehensive studies of transition metal oxides by Biesinger et al. and Chuang et al., providing detailed fitting parameters for various transition metal compounds [43, 44]. The strongly increasing covalency of the Co-O bonding within the perovskite crystal lattice, going from divalent to trivalent cobalt-oxygen bonds results in an inverse shift to lower binding energies with increasing oxidation state of cobalt compounds [45–47], compared to the commonly observed shift to higher binding energies. The magnitude of the Co 2p spin orbit splitting for the LSCO thin films was determined as $\Delta_{BE_{sos}} \approx 15.6$ eV, whereas a separation of $\Delta_{BE_{sos}} \approx 15.2$ eV was determined for the target material.

The Sr 3d core level spectrum exhibits only one single peak related to the perovskite lattice including the non-resolved $3d_{5/2}$ and $3d_{3/2}$ signals at binding energies of BE $\approx$ 132.3 eV and BE $\approx$ 134.0 eV [38]. The more complex La 3d spectrum exhibit a double peak, caused by multiplet splitting of the $3d_{5/2}$ signal. Here peaks at BE $\approx$ 833.5 eV (red) and BE $\approx$ 837.5 eV (blue) are present.

For the further illustration of the results, it should be noted that ICP-MS provides information about the cation-stoichiometry averaged over the entire film composition, whereas XPS provides additional information (including the oxygen stoichiometry) at the film surface. Consequently the results are given in different percentages.

As can be seen from figure 4.7 (a) bulk stoichiometry is changing with laser fluence. While the cobalt content is decreasing linearly, the amount of lanthanum is growing with increasing laser fluences. Strontium however, is randomly varying around an average value of 20.1 %. The average film composition resulting from ICP-MS analysis is La : Sr : Co: 0.61 : 0.41 : 0.98 what is close to the nominal composition La : Sr : Co: 0.60 : 0.40 : 1.00.

Surface analysis by XPS revealed strong deviations from the bulk stoichiometry. As can be seen from figure 4.7 (b) the LSCO surface is generally enriched in cobalt as well as lanthanum and depleted from strontium relative to the target material. Furthermore the content of cobalt seems to correlate inversely to the oxygen content, while La and Sr are not affected by this trend.

This correlation between oxygen and cobalt content is also reflected at lower information depths (figure 4.7 (c)). Furthermore, it can be seen that also the target material shows lower contents of oxygen due to the stronger influence of termination layer with smaller take-off angles. Consequently the relative contents of the other elements are rising by an equal proportion. At this upper surface, oxygen and cobalt content of the the thin films are in the same range as target material, while lanthanum is enriched in and strontium is depleted from the surface relative to the target. Increased scattering of the measured contents relative to (b) can be explained by the lower take-off angle and consequently less intensive signals.

The strong deviation of the thin film grown at a laser fluence of 2.19 J·cm^{-2} relative to the other measurements is caused by a contamination of the surface probably due to an organic

compound, confirmed by an intensive carbonate peak in the O 1s spectrum and can be neglected in the further discussion.

The ratio between trivalent and divalent cobalt plotted against laser fluence is shown in figure 4.8. As described above, the content of trivalent cobalt is reflected by the peak area of the signal at a binding energy of BE $\approx$ 779.6 eV. The divalent cobalt however is reflected by the sum of peak areas of the four residual curves of the Co $2p_{3/2}$ signal. This is due to the fact multiplet splitting does not occur in trivalent cobalt compounds [44, 48] and several investigations had shown that the satellite structure is mainly originating from divalent cobalt compounds [35, 40, 41, 49, 50]. In order to simplify the quantification, the satellite structure is assumed to be solely related to the divalent cobalt content. As shown in figure 4.8 the ratio between trivalent and divalent cobalt obtained from measurements of the target material is around 0.95 for take-off angles of 76 degrees (blue line) and 0.76 for take-off angles of 26 degrees (yellow line), while the average ratio determined for LSCO thin films is independent from information depth ranging around 0.75.

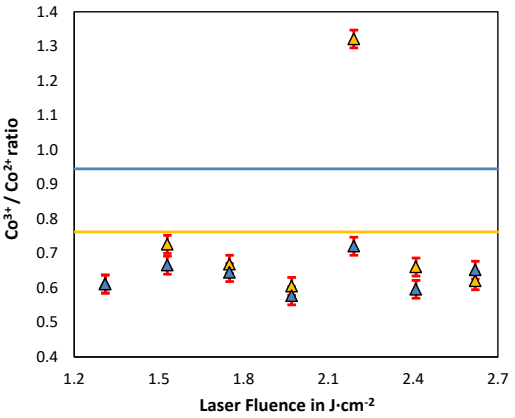

Figure 4.8: Ratio of trivalent and divalent cobalt in the near-surface region obtained by deconvolution of the CO $2p_{3/2}$ core-level signal. The blue solid line denotes the ratio of trivalent and divalent cobalt determined from the target material at a take-off angle of 76 degrees, while the yellow solid line denotes the ratio obtained from measurements at 26 degrees. Triangles denote determined ratios for LSCO thin films grown at various laser fluences, where the colours denote the take-off angle during the measurement equal to the measurements of target material.

4.2 Catalytic performance of LSCO thin films on oxygen evolution reaction

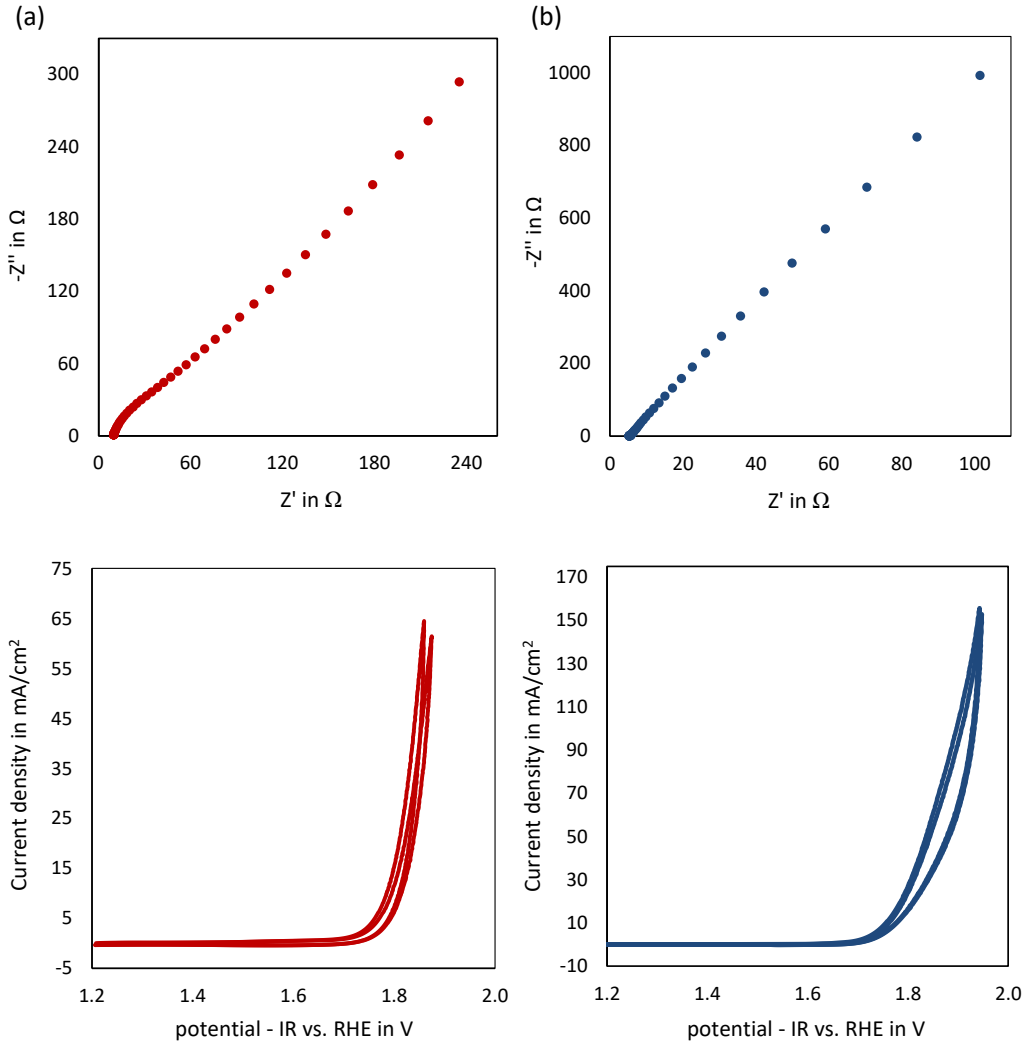

Figure 4.9: Nyquist-plot and cyclic voltagram (below) for epitaxial LSCO thin film electrodes with a thickness of around 100 nm deposited on NGO with a laser fluence of (a) 1.97 J·cm^{-2} and (b) 2.41 J·cm^{-2}. The cyclovoltagrams show two sweeps of potential respectively, where CV data were iR-corrected by the total ohmic serial resistance R_Ω obtained from electrochemical impedance spectroscopy. All measurements were performed with nitrogen-purged 1 M KOH.

Based on the previous investigations, LSCO thin films were fabricated under optimized laser fluence of (a) 1.97 J·cm^{-2} and (b) 2.41 J·cm^{-2} reflecting the lower and higher energy limit where films of defined terrace structures were obtained. In order to test their catalytic properties regarding oxygen evolution reaction, electrochemical experiments provide characteristic values for overpotential, exchange current density and Tafel slope which are of particular importance for the evaluation of the catalytic performance. In figure 4.9 results of EIS and CV measurements obtained from the two epitaxial LSCO thin film samples are illustrated.

The Nyquist-plot reveals in both cases a well defined linear relationship between imaginary and real part of impedance. While for (a) an additional moderate semi-circular region can be

observed at high AC frequencies (close to coordinate origin), no such variation from the linear trend was determined for (b). The linear behaviour accosiated with Warburg impedance (see section 2.4.3.3) is indicating a low charge-transfer resistance and consequently a high catalytic activity towards the oxygen evolution reaction. The linear relationship reflects the strong control of the reaction by mass-transfer. The (weakly defined) semi-circular region in 4.9 (a) reflect a small effect of charge-transfer resistance. The total ohmic serial resistance of the electrolysis cell was determined from the Nyquist-plot, as described in section 2.4.3.3. Here a resistivities of $R_\Omega = 5\,\Omega$ and $R_\Omega = 9.7\,\Omega$ were determined for (a) and (b) respectively.

The measured cyclovoltagrams show the intrinsic current density, plotted against the corresponding applied potential. Here the current density is normalized to a surface area of one square centimeter and the potential is referenced to the reversible hydrogen electrode potential. For both thin films, current density is increasing above about 1.7 V, indicating increased reaction rates at their surface due to oxygen evolution. Conventionally the overpotential is given at a current density of 40 mA·cm^{-2}, where values of 600 mV, as difference to the equilibrium potential of 1.23 V were observed for both LSCO samples. Significant differences are displayed related to the yielded current density, where one of the thin films yielded up to 65 mA·cm^{-2} (4.9 (a)) while the other lead to higher values of around 155 mA·cm^{-2} (4.9 (b)) in the range of applied potential.

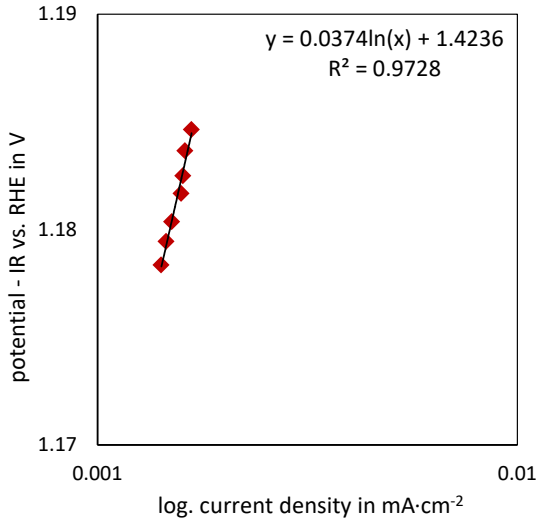

Figure 4.10: Tafel-plot for OER performed on epitaxial LSCO thin film electrodes with a thickness of around 100 nm deposited on NGO with a laser fluence of 1.97 J·cm^{-2} obtained from quasi-reversible voltametry. The CV data was iR-corrected by the total ohmic serial resistance R_Ω obtained from electrochemical impedance spectroscopy. All measurements were performed with nitrogen-purged 1 M KOH.

As an additional indicator for the catalytic activity of LSCO thin films with respect to the oxygen evolution reaction the Tafel slope is determined. For a conservative estimation of the Tafel slope quasi-reversible linear sweep voltametry was performed on the less active sample discussed above. For quasi-reversible measurements, the potential applied to the thin film is held constant at a defined value just above the equilibrium potential, while the exchange current is determined. By successively increasing the potential in defined steps the exchange current is determined for different potentials, where the resulting, ideally linear relation reflect the Tafel-slope. As shown in figure 4.10 a slope of 37 mV·dec^{-1}, reflecting the sensitivity of reaction rate at the catalyst surface to changes in the applied potential, was determined.

4.3 Degradation of LSCO thin films during OER

The study of thin film degradation as a result of catalysis, including morphologic, crystallographic and stoichiometric measurements was initialized. Moreover changes in the average cobalt valency was determined from a film to examine potential impacts of the catalytic process.

Analogous to the variation in catalytic performance differences in degradation behaviour were recognized for the two samples discussed in section 4.2. While a dark circular stain was visible at the contact area to the electrolyte for some samples, only minor changes in colour were observed for others. As can be seen from the AFM images, the surface morphology of the thin film grown at a lower fluence has strongly changed upon the catalysis process. A heterogeneous surface with high roughness is displayed in 4.11 (a). Furthermore several cracks can be observed at the surface of regions of high topography. From comparison of the diffractograms recorded around the (002) peaks an increasing period of thickness oscillation can be seen indicating an decrease in film thickness around $\Delta\, t = 10$ nm after electrochemical processing. The film grown at higher fluences (figure 4.11 (b), however shows no increase in surface roughness. Only a few 3D-features can be observed at the surface. Also the crystallographic orientation seems to be preserved after catalysis, albeit no thin film peak is detected in x-ray diffractometry. Nevertheless an additional scattering signal is displayed as broad feature at lower diffraction angles relative to the substrate peak. In wide-angle x-ray diffractograms this peak of changed position appears at all (001), (002), (003) signals and by this may indicate a persistent epitaxial layer with enlarged c-lattice relative to the original material.

From ICP-MS analysis of a sample after electrochemical processing, an equal content of cobalt (49 %), but decreased contents of both, strontium and lanthanum of 2 % relative to a sample fabricated under equal conditions were observed. Due to the fact the determined deviations were close to the range of error and of course because of a single measurement the results have to be taken with care.

For analysis of changes in surface composition, XPS core-level spectra of post-catalysis samples were recorded as illustrated in figure 4.12. Due to the low quality of spectra recorded with a take-off angle of 26 degrees only spectra recorded at take-off angles of 76 degrees were analyzed. All spectra display changes in peak shape and / or peak position as compared to the as-grown samples. In the O 1s spectrum a dominant peak at higher binding energies relative to the original perovskite peak and with a shoulder to lower binding energies can be observed. According to refs. [40,51], this compound, with an binding energy of of 531.2 eV, may be assigned to $Co(OH)_2$ or $La(OH)_3$. The shoulder of lower intensity can be seen at 529.2 eV, which can not clearly be identified but is probably related to a metal oxide related to the original perovskite peak.

In the cobalt spectrum a slight shift of the main peak to higher binding energies as well as a decrease in peak width relative to the spectrum of pristine LSCO films can be recognized. Besides a shoulder to lower binding energies caused by trivalent cobalt species at BE $\approx$ 779.6 eV illustrated in red, two multiplet peaks at BE $\approx$ 779.4 eV in blue and BE $\approx$ 782.2 eV in green related to divalent cobalt present as $Co(OH)_2$ are shown. Furthermore an increased satellite structure

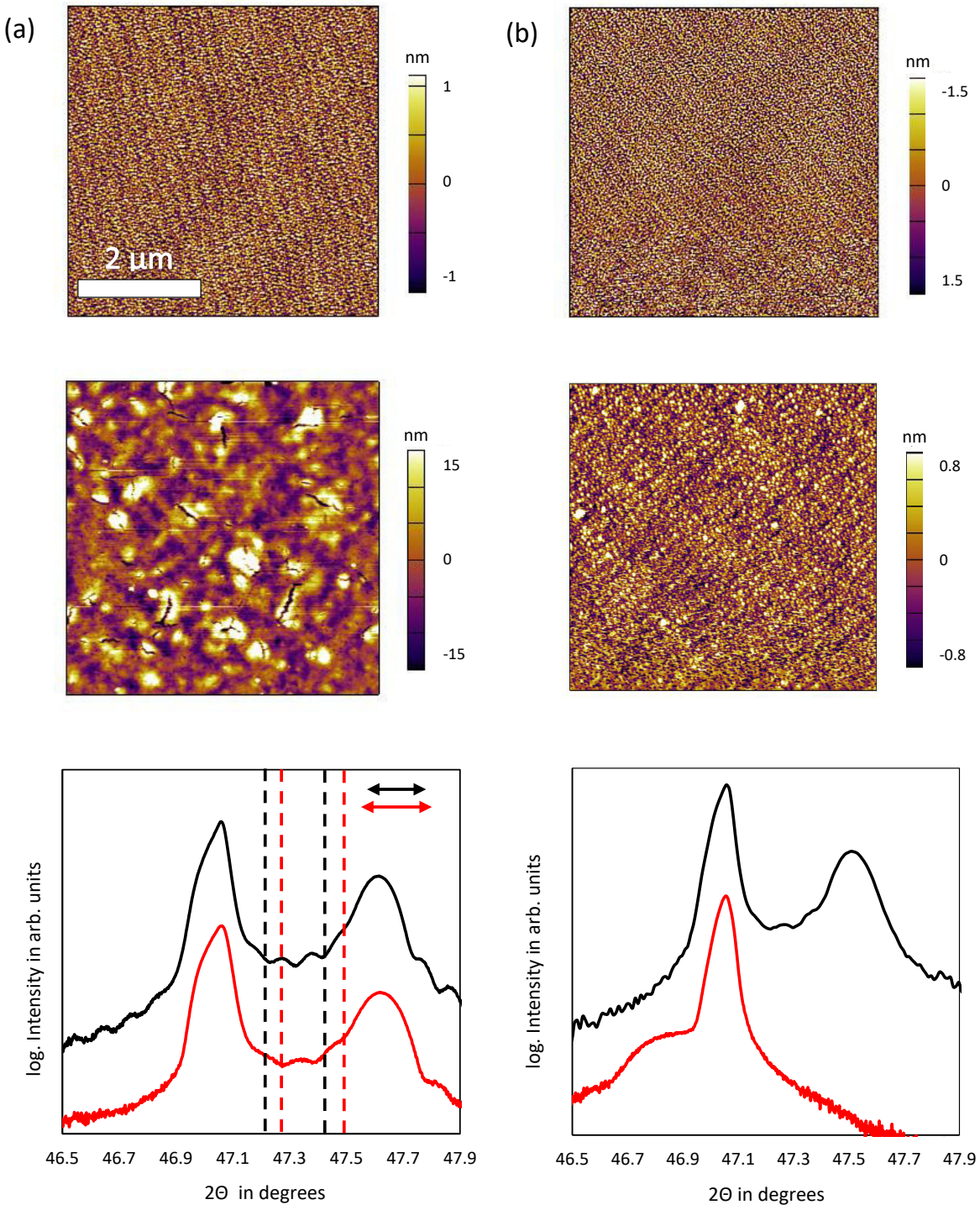

Figure 4.11: From top to bottom: AFM images of pristine thin film, AFM images after electrochemical measurements and diffractograms recorded in 2Θ/Θ-geometry around the (002) substrate peak for LSCO thin films grown at (a) 1.97 J·cm^{-2} and (b) 2.41 J·cm^{-2} after catalysis experiments. In the diffractogram the black curves illustrate diffractogram measured previous to the catalysis, while red curves illustrate the diffractogram after catalysis.

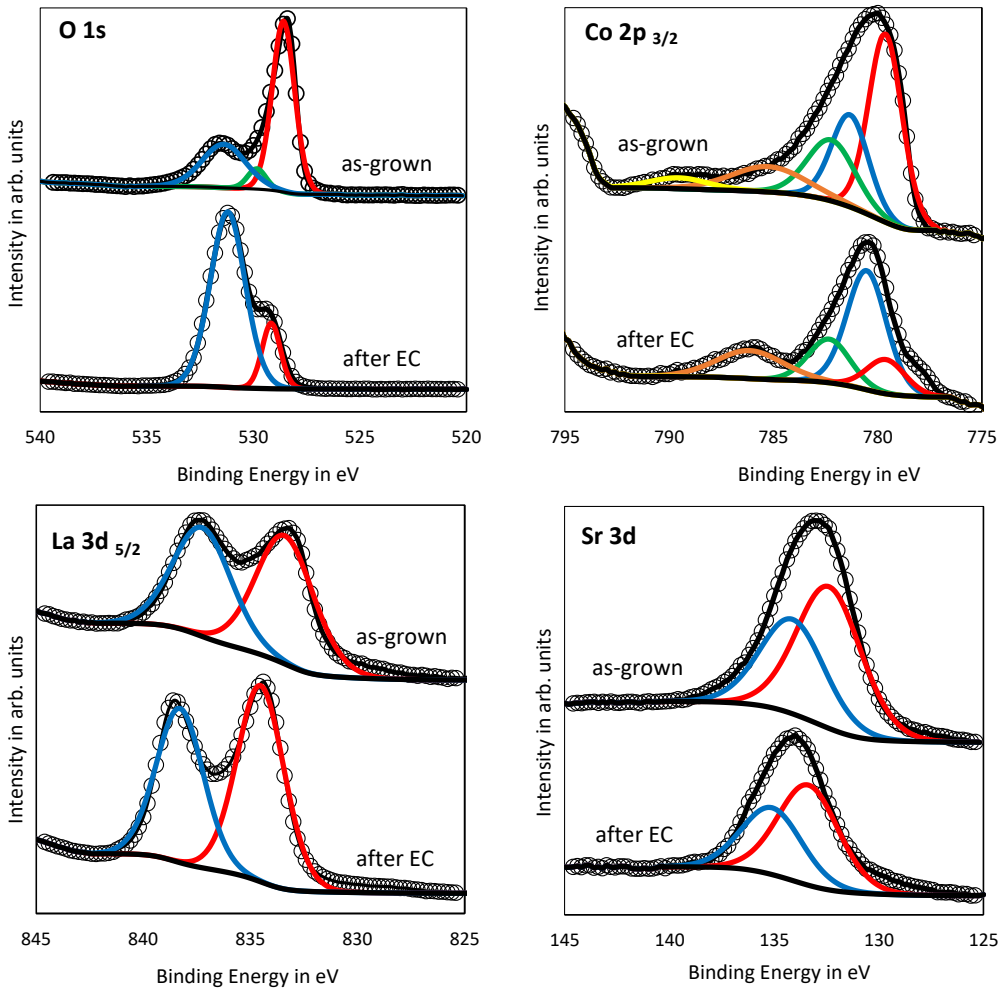

Figure 4.12: Representative O 1s, Co 2p, La 3d and Sr 3d core-level spectra for pristine LSCO thin films and after application for catalysis experiments below, obtained by photoelectron spectroscopy. Colours and symbols for pristine films are equal to figure 4.6. In the O 1s spectrum, the component shown in blue is dedicated to cobalt hydroxide, while the red curve is assingned to an unidentified metal oxide, probably related to the original perovskite peak. In the cobalt spectrum, here limited to the $2p_{3/2}$ signal, the trivalent cobalt is shown in red, the two peaks assigned to divalent cobalt are shown in blue and green and the satellite peaks are shown in orange and yellow respectively. In the La 3d spectrum two peaks related to the La $3d_{5/2}$ signal are shown in red and blue. In the strontium spectrum the overlapping $3d_{5/2}$- and $3d_{3/2}$-signals are shown in red and blue respectively. It should be noted that same colours do not necessarily represent same compounds.

dominated by the peak at BE ≈ 786.0 eV while the intensity of the second satellite observed in the spectrum of pristine thin films is practically not existent. Moreover, a higher magnitude of spin-orbit splitting between Co $2p_{3/2}$ and Co $2p_{1/2}$ main peaks relative to the pristine films of $\Delta_{BE_{sos}} \approx 15.8$ eV was observed.

Both, lanthanum and strontium peaks display shifts to higher binding energies, while the magnitude of multiplet and spin-orbit splitting is equal to the pre-catalysis measurements. The lanthanum multiplet peaks denoted in red and blue can be observed at BE ≈ 834.5 eV and BE ≈ 838.3 eV respectively. The strontium $3d_{5/2}$ (red) and $3d_{3/2}$ (blue) signals are displayed at binding energies of BE ≈ 132.3 eV and BE ≈ 134.0 eV. Equally to the pre-catalysis analysis, the ratio between trivalent and divalent cobalt was determined as 0.11.
The quantification of compounds reflect strong deviations in the film composition, where an increase in the signals of lanthanum (∼25 %) and oxygen (∼36 %) as well as a decrease in the signals of strontium (∼-66 %) and cobalt (∼-55 %) were detected.

5 Discussion

This chapter provides an interpretation and discussion of the results obtained from the thin film studies illustrated in section 4. Here the discussion follows the same chronological order of thin film growth, pre-catalysis thin film characterization, catalysis experiments and degradation studies, as in the previous section.

Investigation of growth mode and surface morphology

The distinct oscillations of RHEED intensity indicates an initial 2D layer-by-layer growth of the perovskite thin film. The following damping of RHEED oscillations reveals second layer nucleation and consequently an increase in surface roughness. The absence of intensity oscillations in the further growth process is an indicator for either island- or step flow growth. However, based on the constant intensity during further deposition 3D growth can be excluded. The increase in the circumference of the Laue-circle reflect the decrease in lattice spacing from substrate to thin film material. More importantly the intensity of the weak streaks observed in the initial state are strongly enhanced and additional spots of varying intensity appeared, both phenomena are clear indicators for a slight roughening of the thin film surface. This coincides with a general increase in intensity of all diffraction spots. Equally the increase in spot sizes are indicating deviations from a perfectly smooth surface due to accumulation of small islands and defects such as advacancies during growth.

The observations based on RHEED were confirmed by the investigation of surface morphology. Highly defined terrace step structures observed for thin films grown with laser fluences between 1.97 $J{\cdot}cm^{-2}$ and 2.41 $J{\cdot}cm^{-2}$ are clearly indicating a 2D growth mode, since the initial surface structure of the substrate is visible even after a growth of around 250 unit cells. Additional diffraction spots in the RHEED pattern are consistent with a slight grain structure on the terrace steps.

The distinct 3D-features on film surfaces grown at unfavourable high or low laser fluences may form as a result of off-stoichiometric growth. It is well known that elemental distribution of adatoms is strongly affected by either discrimination effects during ablation and mass-depending scattering processes within the plasma plume [52, 53]. Here, among other parameters laser fluence is of particular importance. As a result defective growth can lead to a disordered crystal lattice and consequently to a roughened surface.

Crystallographic analysis

Wide-angle XRD investigations, showing only signals from NGO and LSCO that belong to (001) orientation confirm the epitaxy and by this the growth of perovskite phase LSCO films. In addition to that more detailed measurements in the vicinity of the (002) peaks provide further insights in the characteristics of film growth. On the one hand finite thickness fringes give clear evidence of highly crystalline order and coherence of the crystallographic planes of the thin films. Additionally oscillations in the same order of magnitude indicate a similar thickness of the films, confirming the deposition rates determined by means of RHEED intensity in the initial growth phase (table 4.1). On the other hand a severe shift to smaller diffraction angles and consequently larger c-lattice constants with increasing laser fluence can be seen from the diffractograms. This is contrary to the expectations regarding tensile strain epitaxy as described in section 2.2. In this case only films grown at low laser fluences up to 1.8 $J \cdot cm^{-2}$ exhibit slightly decreased c-lattice constants.

Such shifts are often related to stoichiometry as shown by systematic variations of the cation ratio for a related material class (LSCFO) by Kuhn et al. [18]. Due to the lower charge of strontium relative to lanthanum in the crystal lattice, increasing Sr-contents essentially increase the tendency for the formation of oxygen vacancies to ensure charge neutrality. As a consequence of this inherent property LSCO is naturally prone to generate oxygen vacancies, but this property can be influenced by several conditions. Shifts in the lattice parameter are commonly reported for various materials, usually related to oxygen pressure and the resulting difference in formation of oxygen vacancies. Recent studies on LSCO thin films revealed a similar shift with increasing deposition temperatures [39], but generally any parameter with influence to the growth process can lead to variations in the stoichiometry.

Based on the stronger repulsive interaction between adjacent ions of the same charge in consequence of these vacancies, an expansion of the crystal lattice can be the consequence (see chemical expansion parameter in section 2.1. This may even be enhanced with respect to the direct influence of oxygen coordinating cobalt-cations to its valency. The cationic radius of cobalt within the crystal lattice is decreasing with its charge from Co^{2+} to Co^{3+} and Co^{4+} [54]. Due to the fact the (formal) average charge of cobalt as a multivalent ion is decreasing with decrease in coordination number i.e. with enhanced oxygen nonstoichiometry. Hence increased ionic radii of low charged cobalt ions will lead to a even stronger chemical expansion of the crystal lattice as reported for other perovskite oxides [55].

Investigations of the in-plane lattice constants by means of reciprocal space mapping, verified the fully strained growth of the thin films and furthermore confirmed the high quality of epitaxy. Independently from laser fluence two-dimensional reciprocal space maps around the (013) reflection of the substrate revealed signals from NGO and LSCO perpendicular to the x-axis, indicating an adoption in the in-plane lattice spacing.

Electrical analysis

The electrical characterization of the LSCO thin films revealed sheet resistivities in the same order of magnitude independent from laser fluences with a trend to decreased resistivities in the intermediate energy range. With average values between ρ_S = 20 - 30 $\Omega \cdot \square^{-1}$, LSCO revealed exceptionally low resistivities compared to other complex oxides, making the LSCO thin films excellent candidates for electrocatalysis. A high conductivity of the catalyst material is essential for charge transport to the active sites and by this determine the effective potential provided for the charge transfer reaction. While finite conductivity of oxides are frequently a limiting factor in catalysis, LSCO exhibits metallic behaviour, reported to start from $x \geq 0.25$ for $La_{1-x}Sr_xCoO_3$ [56]. Slight deviations in the determined sheet resistivities may be a consequence of small variations in microstructure e.g. crystallinity, defect structure and surface morphology [23]. With respect to the prone character of the material for the formation of oxygen vacancies rather high F-values (close to 1) were determined, indicating a high degree of homogeneity of the thin films as described in section 2.6.

Stoichiometric and chemical state analysis

The bulk stoichiometry determined by means of ICP-MS was shown to be not rather sensitive with respect to laser fluence. All films were grown highly stoichiometric. Only slight changes in the thin film composition, namely an increase in lanthanum content and decrease in cobalt content with increasing laser fluences were observed. This is consistent with theory where elements with low atomic numbers are more strongly affected by scattering with increasing energies within the plasma plume. Consequently a less amount of these elements are deposited on the substrate with the result of slight off-stoichiometric film growth.

This gives a new perspective about the origin of expanding crystal lattice with increasing laser fluence made above. Due to the fact the crystal radius of lanthanum ions are almost twice the size of cobalt ions [54], the increasing content of lanthanum is probably contributing to the increase in lattice spacing.

Photoelectron spectroscopy revealed a general trend to off-stoichiometric surface compositions with higher relative contents of cobalt and lanthanum and depleted from strontium and oxygen compared to the target material ($La_{0.6}Sr_{0.4}CoO_3$). This phenomenon is displayed independently from information depth, albeit the target material shows similar enrichment of cobalt in the upper surface.

This observation of La segregation is contrary to literature, reporting a tendency for strontium segregation in LSCO materials [57]. Also with respect to the strained growth of the thin films, a segregation of the larger ions, namely strontium [54] would be expected. However, this effect remains to be elucidated by further studies. Oxygen deficiency however is rather common for complex oxides and difficult to compare with the target material, due to the fact oxygen is mainly incorporated from the ambient oxygen gas during the growth and not determined by

target composition.

The average cobalt valency was shown to differ from target material, where higher amounts of divalent cobalt in all LSCO thin films were determined by means of areas of the fitted curves. Here equal values were observed for LSCO thin films independent from laser fluence as well as information depth of the analysis, ranging around the values determined for the upper surface of the target. Due to the unsaturated character of surface atoms this may reflect a general oxygen deficient growth of the thin films, also confirmed by the lower oxygen signal relative to the target. Furthermore higher lanthanum contents observed in the near-surface region increase the effective charge in the perovskite and may favour the presence of cobalt ions of decreased valency.

Additionally the decrease in cobalt valency from target to film material is reflected by the increase in the magnitude of spin-orbit splitting. With reference to the literature, the separation of the Co $2p_{3/2}$ and Co $2p_{1/2}$ peak is indicative for the cobalt valence, where larger separations indicate higher contents of divalent cobalt. Vice versa lower magnitudes of splitting are related to cobalt compounds of higher valency [44, 46, 48, 50, 58]. The increasing spin-orbit separation from target to thin film material reflects the decrase in average cobalt valence.

In summary, in-plane strained LSCO thin films of specific thicknesses were deposited in 2D-growth mode, where the out-of-plane lattice constant was shifted to larger values with increasing laser fluences. Under optimal laser fluences the thin films exhibited highly defined surfaces, with a discernible terrace structure and lower surface roughness compared to the literature [12, 13, 59] in a wide range of laser fluences. All thin films revealed highly stoichiometric compositions in bulk. Only slight but constant deviations from stoichiometry were found in the near-surface region, namely higher lanthanum and lower strontium contents. Additionally, the O 1s photoelectron spectrum indicate an oxygen deficient surface. Furthermore the thin films showed only negligible deviations in their generally low sheet resistivities. By this an ideal, highly defined system regarding to morphology. crystallography, stoichiometry and electrical properties was obtained for the study of electrocatalysis of OER.

Electrochemical analysis

Based on electrochemical measurements the suitability of epitaxial LSCO thin films to catalyze the anodic OER was confirmed. By means of EIS a mass-transfer controlled process was observed. The total ohmic serial resistance between R_Ω = 5 - 10 Ω reveals, consistent with low sheet resistivity, high electrical conductivity. While thin film resistivity was described as bottleneck for the electron transport to the active sites before, the low serial resistance indicates no limitation based on film resistivity.

The onset voltage of OER current, indicating the potential necessary to overcome the kinetic barrier for the OER was observed at around 1.7 V as earlier reported for cobalt based catalysts [7] but significantly higher than reported for LSCO powder of the same stoichiometry [21].

Due to the lack of sufficient reference data for current densities at defined overpotentials obtained from epitaxial thin films measured under similar experimental conditions, comparison to the literature is difficult. In comparison to a PBCO ($Pr_{0.5}Ba_{0.5}CoO_3$) thin film of same thickness and analyzed under equal conditions, significantly higher current densities were measured. At overpotentials of 600 mV LSCO thin films were more than ∼15-times more active than the PBCO catalyst. Reflecting the intrinsic interaction between catalyst and reactant these high current densities are clearly indicating an excellent catalytic performance of LSCO for the OER.

Furthermore the determined Tafel slope was lower than reported in the literature as 64 $mV \cdot dec^{-1}$ for $La_{0.6}Sr_{0.4}CoO_3$ [60] and related cobalt-based catalysts (LSFCO: 80 $mV \cdot dec^{-1}$, LCO: 70 $mV \cdot dec^{-1}$, Co_3O_4 [5]). Since efficient catalysis requires strongly increasing current density by small changes in overpotential, small Tafel slopes are favourable for electrocatalysis. According to the literature the magnitude of Tafel slope is furthermore an indicator for the catalysis mechanism, hence it is related to the determining step of the multi-step reaction. Low values of Tafel slope indicate a rate-determining step proceeding later on in the multi-step reaction, where Tafel slopes of 120 $mV \cdot dec^{-1}$, 60 $mV \cdot dec^{-1}$ and 30 $mV \cdot dec^{-1}$ are corresponding to the first, second and third electron-transfer reaction of the overall reaction [5]. Based on this information, the measured Tafel slope could be assigned to a rate-determining step by the third electron transfer whereas Bockris et al. determined a Tafel slope corresponding to a OER reaction rate determined by the second electron transfer. This deviation may indicate differences in the catalysis mechanism between powder and thin film catalysts providing different crystallographic sites for the catalysis process. Moreover, the oxygen deficiency of the thin films might be of importance, as their great influence to the catalytic mechanism was shown by Mefford et al. by successive Sr-doping of LSCO.

However, the small number of samples does not provide a convincing basis for wide interpretations, but it should be considered for further investigations.

Investigation of thin film degradation

Also a variation in degradation behaviour was found for the different films. While one of the thin films showed a significant roughening of the surface, another one revealed almost unchanged morphology. Equally, the way of degradation, observed as simple decrease in thickness or alternatively as amorphization of the thin film with a resulting loss of XRD signal was strongly varying. Here too, an influence of the surface deficiency could be the reason. As predicted from theoretical considerations surface deficiency, besides aqueous conditions and applied potential, is with high impact to the stability and activity of oxide catalysts [61].

Subsequent to catalysis the cobalt spectrum clearly reflects a change in the average cobalt valence to lower values due to the catalytic process. While the content of trivalent cobalt, corresponding to the red curve is significantly decreased, signals related to multiplet splitting of divalent cobalt dominate the peak shape, what is resulting from a strongly decreased ratio of trivalent to divalent cobalt. Furthermore the magnitude of spin-orbit splitting was increased further on compared to

separations of target as well as pristine LSCO thin films. Furthermore, the shift in the peaks related to divalent cobalt to positions reflecting the presence of cobalt hydroxide is consistent with the decreased valency.

However, due to the film degradation these findings reflect not the properties of the intact catalyst, but the chemistry of degradation products. Due to the fact the increase in lanthanum and oxygen content are scaling with each other it can be expected that the major proportion of the hydroxide peak, observed in the O 1s spectrum, is related to a lanthanum compound. Here A-site leaching, as previously reported for perovskite catalysts during cyclic voltametry [8], with the subsequent formation hydroxides may have occurred. Whereas to the strontium hydroxide may have dissolved due to its finite solubility [62].

6 Conclusions

For the study of OER electrocatalysis on LSCO, high quality and well defined $La_{0.6}Sr_{0.4}CoO_3$ thin films of constant thickness were grown by PLD on NGO and studied on multiple levels. Here a detailed overall picture of the thin film material was gained by means of various complementary techniques.

The two-dimensional deposition was dominated by initial layer-by-layer and subsequent step-flow mode. The 2D growth mode was consistent with morphological investigations, revealing low surface roughness of RMS < 0.6 nm at laser fluences between 1.97 J·cm^{-2} and 2.41 J·cm^{-2}. Crystallographic studies confirmed the epitaxy of the perovskite thin films. Stoichiometric investigations of bulk and surface of the thin films confirmed the high accuracy to the targeted stoichiometry. The electrical characterization revealed the extraordinarily high conductivity of the LSCO thin films as complex oxide material.

By this comprehensive material characterization, perovskite-type cobaltite thin film catalysts with nearly atomically flat surfaces, defined crystal lattice parameters, specific stoichiometry and metallic conductivity was obtained as well-suited system for the investigation of the catalytic process during water splitting and its impact to the material. Pioneering experiments regarding to OER catalysis using epitaxial LSCO thin films provided information about the high catalytic performance of the thin film material. A significantly enhanced catalytic activity compared to other epitaxial cobaltite thin film catalyst, apparent from high current density up to 155 mA·cm^{-2} during oxygen evolution and a low Tafel slope of 37 mV·dec^{-1} was observed, characterizing LSCO as an ideal model material for systematic studies on the atomic processes during OER.

Furthermore a model for deconvolution of the complex Co 2p core-level spectrum was developed, qualified for the determination of relative changes in the average cobalt valency. Based on this model differences in the average cobalt valency of the target material as well as the thin film material before and after catalysis experiments were determined, providing information about changes in the materials properties due to the deposition as well as the catalytic process.

In the same context the limitation of this approach to investigate the catalytic process was shown. Degradation of the perovskite phase due to leaching effects and the formation of cation hydroxides lead to an altered system which is difficult to compare with the original material. This illustrates the importance of high stability for the application of catalytic thin films as model systems for the study of specific descriptors for the catalytic activity.

7 Outlook

The developed cobaltite catalyst system and curve fitting model opens new opportunities to continue with systematic investigations of the water splitting process. Various approaches could be followed for the further investigation in the material properties with respect to catalytic activity, stability as well as the nature of cobalt valency. Here, additional studies of the thin film stability, for instance by end of service life tests, as reported elsewhere [8], could be beneficial to understand the degradation process.

For instance the concentration of oxygen vacancies could be tuned by variation of deposition parameters to investigate the catalytic activity as a function of surface defects. Furthermore the fabrication of epitaxial thin films by deposition on substrates with different lattice misfit to the LSCO crystal structure could be used for the strain-induced variation of lattice spacing. This might provide information about the adsorbative behaviour of OER intermediates and hence about the dependency of the catalytic activity on the atomic spacing at the thin film surface. Another option could be, to grow films in different crystallographic orientations and to provide different termination layers of the crystal for the catalytic process.

Due to the very smooth surface of the thin films, alternative approaches for the investigation of catalyst reactant interaction, such as STEM could be used to study the role of oxygen vacancies for the behaviour of adsorbates at the catalyst surface on the atomic scale. Also the application of photoelectron microscopy, might provide additional information about the degradation process due to its lateral resolution. Studies after the catalytic process, could be useful to investigate leaching processes with respect to surface properties of the catalytic thin films.

List of Abbreviations

AFM	Atomic Force Microscopy
CV	Cyclic Voltametry
EIS	Electrochemical Impedance Spectroscopy
FWHM	Full Width Half Maximum
HER	Hydrogen Evolution Reaction
LSCO	Lanthanum strontium cobalt oxide
NGO	Neodymium gallate
OER	Oxygen Evolution Reaction
PLD	Pulsed Laser Deposition
RHEED	Reflection high-energy electron diffraction
RSM	Reciprocal space mapping
RSM	Root Mean Square
RSF	Relative Sensitivity Factor
XRD	X-Ray diffraction

List of Figures

List of Tables

Acknowledgements

First of all I would like to thank Prof. Clemens Walther and Prof. Regina Dittmann for agreeing to supervise and review my thesis and in this way, giving me the opportunity to complete my Master studies in Jülich.

Furthermore I'd like to thank Christoph Bäumer and Michael Andrä for the helpful discussions about photoelectron spectroscopy, as well as David Müller for sharing his knowledge with me in several meetings.

Many thanks also to Daniel Bick for his support and guidance during my electrochemistry experiments in Aachen.

Special thanks to Paul Meufels, René Borowski, Georg Pickartz, Jochen Friedrich and Mirka Grates for their technical support and of course thanks to all the other colleagues from PGI-7 who welcomed me so friendly at the institute.

I would particularly like to thank Felix Gunkel for his mentoring and his generous support during my whole time in Jülich. Special thanks for his great support even after becoming a father for the first time.

Finally I want to thank my family for always encouraging and supporting me - and, most importantly, Mia for her love and her patience with me during my studies.

Bibliography

[1] U.S. Energy Information Administration. International Energy Outlook. *Independent Statistics & Analysis* , ():, 2016.

[2] Varone, A. & Ferrari, M. Power to liquid and power to gas: An option for the German Energiewende. *Renewable and Sustainable Energy Reviews*, 45():207–218, 2015.

[3] Ellabban, Omar and Abu-Rub, Haitham and Blaabjerg, Frede. Renewable energy resources: Current status, future prospects and their enabling technology. *Renewable and Sustainable Energy Reviews*, 39(49):748–764, 2014.

[4] Hong, Wesley T. and Risch, Marcel and Stoerzinger, Kelsey A. and Grimaud, Alexis and Suntivich, Jin and Shao-Horn, Yang. Toward the rational design of non-precious transition metal oxides for oxygen electrocatalysis. *Energy Environ. Sci.*, 8(5):1404–1427, 2015.

[5] Suen, Nian-Tzu and Hung, Sung-Fu and Quan, Quan and Zhang, Nan and Xu, Yi-Jun and Chen, Hao Ming. Electrocatalysis for the oxygen evolution reaction: recent development and future perspectives. *Chem. Soc. Rev.*, 46(2):337–365, 2017.

[6] Chen, Dengjie and Chen, Chi and Baiyee, Zarah Medina and Shao, Zongping and Ciucci, Francesco. Nonstoichiometric Oxides as Low-Cost and Highly-Efficient Oxygen Reduction/Evolution Catalysts for Low-Temperature Electrochemical Devices. *Chemical Reviews*, 115(10):9869–9921, 2015.

[7] Felix Gunkel, Lei Jin, David N. Mueller, Clemens Hausner, Daniel S. Bick, Chun-Lin Jia, Theodor Schneller, Ilia Valov, Rainer Waser, and Regina Dittmann. Ordering and Phase Control in Epitaxial Double-Perovskite Catalysts for the Oxygen Evolution Reaction. *ACS Catalysis*, 7(10):7029–7037, 2017.

[8] Bick, D. S. and Kindsmueller, A. and Staikov, G. and Gunkel, F. and Mueller, D. and Schneller, T. and Waser, R. and Valov, I. Stability and Degradation of Perovskite Electrocatalysts for Oxygen Evolution Reaction. *Electrochimica Acta*, 218(6):156–162, 2016.

[9] Chang, Seo Hyoung and Danilovic, Nemanja and Chang, Kee Chul and Subbaraman, Ram and Paulikas, Arvydas P. and Fong, Dillon D. and Highland, Matthew J. and Baldo, Peter M. and Stamenkovic, Vojislav R. and Freeland, John W. and Eastman, Jeffrey A. and Markovic, Nenad M. Functional links between stability and reactivity of strontium ruthenate single crystals during oxygen evolution. *Nature Communications*, 5(1):1–9, 2014.

[10] Stoerzinger, Kelsey A. and Seok Choi, Woo and Jeen, Hyoungjeen and Lee, Ho Nyung and Shao-Horn, Yang. Role of strain and conductivity in oxygen electrocatalysis on LaCoO3 thin films. *Journal of Physical Chemistry Letters*, 6(3):487–492, 2015.

[11] Scholz, Julius and Risch, Marcel and Stoerzinger, Kelsey A. and Wartner, Garlef and Shao-Horn, Yang and Jooss, Christian. Rotating Ring–Disk Electrode Study of Oxygen Evolution at a Perovskite Surface: Correlating Activity to Manganese Concentration. *The Journal of Physical Chemistry C*, 120(49):27746–27756, 2016.

[12] Kubicek, Markus and Limbeck, Andreas and Frömling, Till and Hutter, Herbert and Fleig, Jürge. Relationship between Cation Segregation and the Electrochemical Oxygen Reduction Kinetics of La0.6Sr0.4CoO3δ Thin Film Electrodes. *Journal of The Electrochemical Society*, 158(6):B727, 2011.

[13] Crumlin, E. J. and Ahn, S.-J. and Lee, D. and Mutoro, E. and Biegalski, M. D. and Christen, H. M. and Shao-Horn, Y. Oxygen Electrocatalysis on Epitaxial La0.6Sr0.4CoO3 $-$ δ Perovskite Thin Films for Solid Oxide Fuel Cells. *Journal of the Electrochemical Society*, 159(7):219–225, 2012.

[14] Cai, Zhuhua and Kubicek, Markus and Fleig, Jürgen and Yildiz, Bilge. Chemical Heterogeneities on La _{0.6} Sr _{0.4} CoO _{3δ} Thin Films—Correlations to Cathode Surface Activity and Stability. *Chemistry of Materials*, 24(6):1116–1127, 2012.

[15] P.A. Cox. *Transition Metal Oxides - An Introduction to their Electronic Structure and Properties*. Oxford University Press, New York, USA, 1992.

[16] CrysTec Kristalltechnologie. *$NdGaO_3$ for Research and Development*, 2017.

[17] C. Lenser. *Investigation of Resistive Switching in Fe-doped $SrTiO_3$ by Advanced Spectroscopy*. PhD thesis, RWTH Aachen, Germany, 2013.

[18] Kuhn, M. and Hashimoto, S. and Sato, K. and Yashiro, K. and Mizusaki, J. Thermochemical lattice expansion in $La_{0.6}Sr_{0.4}Co_{1-y}Fe_yO_{3-\delta}$. *Solid State Ionics*, 241:12–16, 2013.

[19] M. Ohring. *The Materials Science of Thin Films*. Academic Press, USA, 1992.

[20] K. Kendall and M. Kendall. *High-Temperature Solid Oxide Fuel Cells for the 21st Century - Fundamentals, Design and Applications*. Elsevier Academic Press, The Netherlands, 2016.

[21] Mefford, J. Tyler and Rong, Xi and Abakumov, Artem M. and Hardin, William G. and Dai, Sheng and Kolpak, Alexie M. and Johnston, Keith P. and Stevenson, Keith J. Water electrolysis on La1xSrxCoO3δ perovskite electrocatalysts. *Nature Communications*, 7(11053):2041–1723, 2016.

[22] P.R. Willmott. Deposition of complex multielemental thin films. *Progress in Surface Science*, 76():163–217, 2004.

[23] G. Rijnders. *The initial growth of complex oxides - Study and Manipulation*. Dissertation, Twente University, 2001.

[24] H.M. Christen, G. Eres. Recent advances in pulsed-laser deposition of complex oxides. *Journal of Physics: Condensed Matter*, 20(26):, 2008.

[25] Peter Eaton, Paul West. *Atomic Force Miscroscopy*. Oxford University Press, UK, 2010.

[26] P. F. Fewster. Reciprocal space mapping. *Critical Reviews in Solid State and Materials Sciences*, 22(2):69–110, 1997.

[27] P. F. Fewster. X-ray analysis of thin films and multilayers. *Reports on Progress in Physics*, 59(11):1339–1407, 1996.

[28] D.K. Schroder. *Semiconductor Material and Device Characterization*. Wiley-Interscience, New Jersey, USA, 2006.

[29] L. J. Van der Pauw. A method of measuring the resistivity and hall coefficient on lamellae of arbitrary shape. *Philips Technical Review*, 20(8):220–224, 1958.

[30] Allen J. Bard, Larry R. Faulkner. *Electrochemical Methods - Fundamentals and Applications*. John Wiley Sons, Inc., Texas, USA, 2001.

[31] Nicholson, Richard S. Theory and Application of Cyclic Voltammetry for Measurement of Electrode Reaction Kinetics. *Analytical Chemistry*, 37(11):1351–1355, 1965.

[32] Ángela Molina, Jouaquín González. *Pulse Voltammetry in Physical Electrochemistry and Electroanalysis - Theory and Applications*. Springer International Publishing AG Switzerland, Switzerland, 2016.

[33] Hofmann, S. *Auger- and X-Ray Photoelectron Spectroscopy in Materials Science - A User-Oriented Guide*. Springer-Verlag Berlin Heidelberg, Germany, 2013.

[34] PHI Customer Service. *VersaProbe - Installation and Calibration Manual*. Physical Electronics, Inc.

[35] Van der Heide, P.A.W. Systematic x-ray photoelectron spectroscopic study of $La_{1-x}Sr_x$-based perovskite-type oxides. *Surface and interface analysis*, 33():414–425, 2001.

[36] Atkins, P.W., De Paula, J. *Atkins' Physical Chemistry*. Oxford University Press, Oxford, UK, 2006.

[37] Nenning, Andreas and Opitz, Alexander K. and Rameshan, Christoph and Rameshan, Raffael and Blume, Raoul and Hävecker, Michael and Knop-Gericke, Axel and Rupprechter, Günther and Klötzer, Bernhard and Fleig, Jürgen. Ambient pressure XPS study of mixed conducting perovskite-type SOFC cathode and anode materials under well-defined electrochemical polarization. *Journal of Physical Chemistry C*, 120(3):1461–1471, 2016.

[38] Crumlin, Ethan J. and Mutoro, Eva and Hong, Wesley T. and Biegalski, Michael D. and Christen, Hans M. and Liu, Zhi and Bluhm, Hendrik and Shao-Horn, Yang. In situ ambient pressure X-ray photoelectron spectroscopy of cobalt perovskite surfaces under cathodic polarization at high temperatures. *Journal of Physical Chemistry C*, 117(31):16087–16094, 2013.

[39] Ethan J. Crumlin, Eva Mutoro, Zhi Liu, Michael E. Grass, Michael D. Biegalski, Yueh-Lin Lee, Dane Morgan, Hans M. Christen, Hendrik Bluhmg and Yang Shao-Horn. Surface

strontium enrichment on highly active perovskites for oxygen electrocatalysis in solid oxide fuel cells. *Energy Environ. Sci.*, 5():6081–6088, 2012.

[40] Mcintyre, N. S. and Cook, M. G. X-Ray Photoelectron Studies on Some Oxides and Hydroxides of Cobalt, Nickel, and Copper. *Analytical Chemistry*, 47(13):2208–2213, 1975.

[41] Vovk, Greg and Chen, Xiaohua and Mims, Charles A. In situ XPS studies of perovskite oxide surfaces under electrochemical polarization. *Journal of Physical Chemistry B*, 109(6):2445–2454, 2005.

[42] H. H. Kung. *Transition Metal Oxides - Surface Chemistry and Catalysis*. Elsevier science puplisher company inc., USA, 1989.

[43] Biesinger, Mark C. and Payne, Brad P. and Grosvenor, Andrew P. and Lau, Leo W M and Gerson, Andrea R. and Smart, Roger. Resolving surface chemical states in XPS analysis of first row transition metals, oxides and hydroxides: Cr, Mn, Fe, Co and Ni. *Applied Surface Science*, 257(7):2717–2730, 2011.

[44] Chuang, T.J. and Brundle, C.R. and Rice, D.W. Interpretation of the x-ray photoemission spectra of cobalt oxides and cobalt oxide surfaces. *Surf. Sci.*, 59(44):413–429, 1976.

[45] Fierro, G. and Dragone, R. and Moretti, G. and Porta, P. XPS investigation on Co-Cu mixed oxide catalysts. *Surface and Interface Analysis*, 19(1-12):565–571, 1992.

[46] Fierro, G and Jacono, M Lo and Inversi, M and Dragone, R and Porta, P. TPR and XPS study of cobalt–copper mixed oxide catalysts: evidence of a strong Co–Cu interaction. *Topics in Catalysis*, 10:39–48, 2000.

[47] D. K. G. de Boer, C. Haas, and G. A. Sawatzky. Exciton satellites in photoelectron spectra.

[48] S. Angelov, G. Tyuliev and Ts. Marnova. XPS study of surface composition of polycrystalline $Cu_xCo_3 - xO_4$ ($0 \tilde{<} x < 1$) obtained by thermal decomposition of nitrate mixtures. *Applied Surface Science*, 27:381–392, 1987.

[49] Natile, Marta Maria and Glisenti, Antonella. Study of surface reactivity of cobalt oxides: Interaction with methanol. *Chemistry of Materials*, 14(7):3090–3099, 2002.

[50] Deng, Jiguang and Zhang, Lei and Dai, Hongxing and He, Hong and Au, Chak Tong. Single-crystalline La0.6Sr0.4CoO3-δ nanowires/nanorods derived hydrothermally without the use of a template: Catalysts highly active for toluene complete oxidation. *Catalysis Letters*, 123(3-4):294–300, 2008.

[51] Sunding, M. F. and Hadidi, K. and Diplas, S. and L??vvik, O. M. and Norby, T. E. and Gunns, A. E. XPS characterisation of in situ treated lanthanum oxide and hydroxide using tailored charge referencing and peak fitting procedures. *Journal of Electron Spectroscopy and Related Phenomena*, 184(7):399–400, 2011.

[52] S. Wicklein, A. Sambri, S. Amoruso, X. Wang, R. Bruzzese, A. Koehl, and R. Dittmann. Pulsed laser ablation of complex oxides: The role of congruent ablation and preferential scattering for the film stoichiometry. *Applied Physics Letters*, 101(131601):, 2012.

[53] R. Groenen; J. Smit; K. Orsel; A. Vailionis; B. Bastiaens; M. Huijben; K. Boller; G. Rijnders; G. Koster. Research Update: Stoichiometry controlled oxide thin film growth by pulsed laser deposition. *APL Materials*, 3(7):, 2015.

[54] R.D. Shannon. Revised Effective Ionic Radii and Systematic Studies of Interatomic Distances in Halides and Chalcogenides. *Acta Crystallographica Section A*, 32(5):751–767, 1976.

[55] Perry, Nicola H. and Bishop, Sean R. and Tuller, Harry L. Tailoring chemical expansion by controlling charge localization: in situ X-ray diffraction and dilatometric study of (La,Sr)(Ga,Ni)O 3δ perovskite. *J. Mater. Chem. A*, 2(44):18906–18916, 2014.

[56] Mineshige, Atsushi and Kobune, Masafumi and Fujii, Satoshi and Ogumi, Zempachi and Inaba, Minoru. Metal–Insulator Transition and Crystal Structure of La1-xSrxCoO3 as Functions of Sr-Content , Temperature , and Oxygen Partial Pressure. *Journal of Solid State Chemistry*, 142():374–381, 1999.

[57] Feng, Zhenxing and Yacoby, Yizhak and Gadre, Milind J. and Lee, Yueh Lin and Hong, Wesley T. and Zhou, Hua and Biegalski, Michael D. and Christen, Hans M. and Adler, Stuart B. and Morgan, Dane and Shao-Horn, Yang. Anomalous interface and surface strontium segregation in $(La_{1-y}Sr_y)_2CoO_{4\pm\delta}/La_{1-x}Sr_xCoO_{3-\delta}$ heterostructured thin films. *Journal of Physical Chemistry Letters*, 5(6):1027–1034, 2014.

[58] Mulinari, Tatiana a. and La Porta, Felipe a. and Andres, Juan and Cilense, Mario and Varela, Jose a. and Longo, Elson. Microwave-hydrothermal synthesis of single-crystalline Co3O4 spinel nanocubes. *CrystEngComm*, 15(37):7443, 2013.

[59] Tsvetkov, Nikolai and Lu, Qiyang and Sun, Lixin and Crumlin, Ethan J. and Yildiz, Bilge. Improved chemical and electrochemical stability of perovskite oxides with less reducible cations at the surface. *Nature Materials*, 15(9):1010–1016, 2016.

[60] Bockris, John O. and Otagawa, Takaaki. Mechanism of oxygen evolution on perovskites. *The Journal of Physical Chemistry*, 87(15):2960–2971, 1983.

[61] Rong, Xi and Kolpak, Alexie M. Ab initio approach for prediction of oxide surface structure, stoichiometry, and electrocatalytic activity in aqueous solution. *Journal of Physical Chemistry Letters*, 6(9):1785–1789, 2015.

[62] Zeng, Y. and Lin, Y.S. and Swartz, S.L. Perovskite-type ceramic membrane: synthesis, oxygen permeation and membrane reactor performance for oxidative coupling of methane. *Journal of Membrane Science*, 150(1):87–98, 1998.